A roadmap for the characterization of energy metabolism in human cardiomyocytes derived from induced pluripotent stem cells.

Giulia Emanuelli[1,2], Anna Zoccarato[1†], Christina M Reumiller[1], Angelos Papadopoulos[1], Mei Chong[1], Sabine Rebs[2], Kai Betteridge[1], Matteo Beretta[1], Katrin Streckfuss-Bömeke[2,*], Ajay M Shah[1*,†]

[1]King's College London British Heart Foundation Centre of Excellence, School of Cardiovascular Medicine & Sciences, London, United Kingdom;
[2]Clinic for Cardiology and Pneumonology, University Medical Center Göttingen, Germany and DZHK (German Centre for Cardiovascular Research), partner site Göttingen, Germany.
*, KS-B & AMS are joint senior authors.

[†]**Correspondence to:** Professor Ajay M Shah and Dr Anna Zoccarato, King's College London School of Cardiovascular Medicine & Sciences, James Black Centre, 125 Coldharbour Lane, London SE5 9NU, UK.
Email: ajay.shah@kcl.ac.uk, anna.zoccarato@kcl.ac.uk
Tel: 44-2078485189; Fax: 44-2078485193

Running title: Metabolic profile of human iPSC-cardiomyocytes

Key words: iPSC-derived cardiomyocytes; energy metabolism; metabolic maturation; cardiac cell models; metabolic shift.

Summary:

Human induced pluripotent stem cell-derived cardiomyocytes (hiPSC-CM) are a promising tool for cardiac disease modeling and drug discovery. Results with this model need to be interpreted in the context of their baseline phenotype. We performed detailed multimodality characterization of the metabolic profile of differentiated hiPSC-CM during progressive maturation. We observed progressive remodeling of pathways of energy metabolism and substrate utilization, including the oxidation of fatty acids, glucose and glutamine, and anaerobic glycolysis. This was paralleled by a maturation of mitochondrial function. This work provides a roadmap for the metabolic changes that occur during hiPSC-CM maturation.

Graphical abstract:

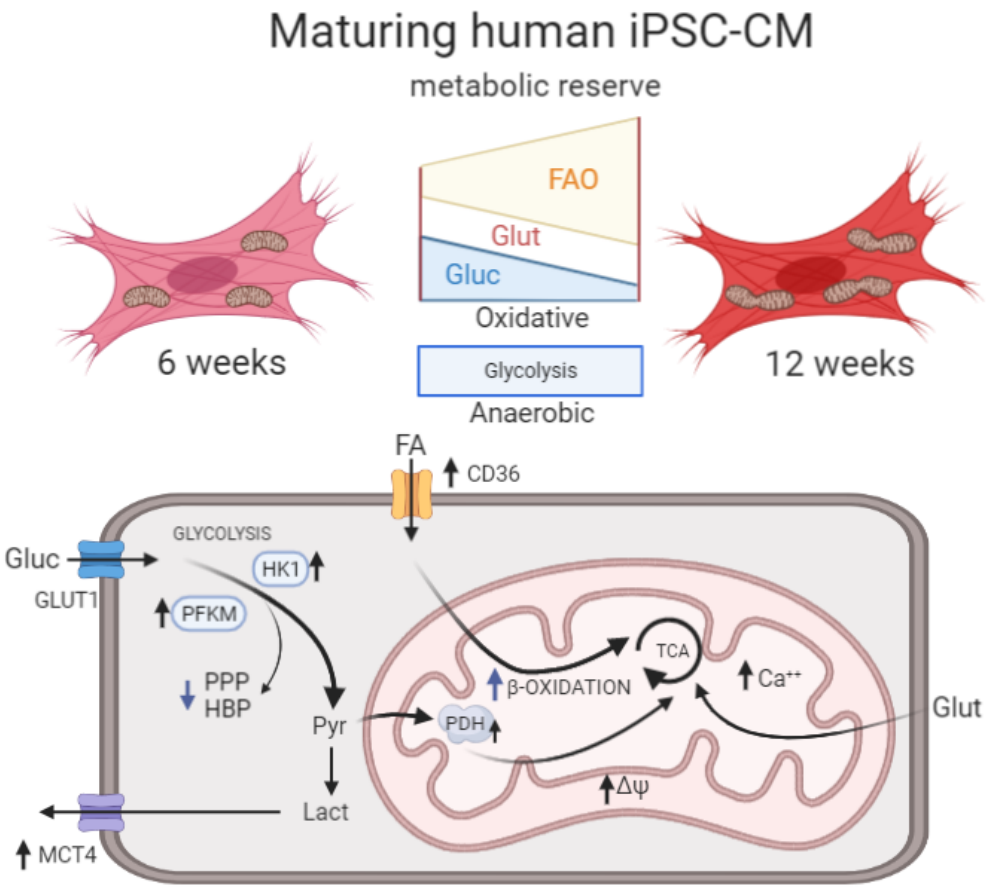

Abstract

Human induced pluripotent stem cell-derived cardiomyocytes (hiPSC-CM) are an increasingly employed model in cardiac research and drug discovery. As cellular metabolism plays an integral role in determining phenotype, the characterization of the metabolic profile of hiPSC-CM during maturation is crucial for their translational application. In this study we employ a combination of methods including extracellular flux, ^{13}C-glucose enrichment and targeted metabolomics to characterize the metabolic profile of hiPSC-CM during their maturation in culture from 6 weeks, up to 12 weeks. Results show a progressive remodeling of pathways involved in energy metabolism and substrate utilization along with an increase in sarcomere regularity. The oxidative capacity of hiPSC-CM and particularly their ability to utilize fatty acids increased with time. In parallel, relative glucose oxidation was reduced while glutamine oxidation was maintained at similar levels. There was also evidence of increased coupling of glycolysis to mitochondrial respiration, and away from glycolytic branch pathways at later stages of maturation. The rate of glycolysis as assessed by lactate production was maintained at both stages but with significant alterations in proximal glycolytic enzymes such as hexokinase and phosphofructokinase. We observed a progressive maturation of mitochondrial oxidative capacity at comparable levels of mitochondrial content between these time-points with enhancement of mitochondrial network structure. These results show that the metabolic profile of hiPSC-CM is progressively restructured, recapitulating aspects of early post-natal heart development. This would be particularly important to consider when employing these cell model in studies where metabolism plays an important role.

Introduction

The ability to derive cardiomyocytes (CM) from induced pluripotent stem cells (iPSC) has opened new avenues for drug discovery and disease modeling using human cells [1]. As early as 4-6 weeks after differentiation from human iPSC, hiPSC-CM exhibit clear features of primary cardiomyocyte structure, electrophysiology, contraction and pharmacological responses to inotropic agents [2]. However, these cells display an overall immature phenotype, with their transcriptome more closely resembling fetal than adult cardiomyocytes [3]. hiPSC-CM retain a higher proliferative potential than adult CM, a less organized sarcomere structure, spontaneous contractile activity and slower action potentials [4]. This immature phenotype constitutes the main limitation to their use in disease modeling and regenerative medicine. As such, considerable efforts have been made to develop strategies to induce faster or increased maturation, including electrical and mechanical activation and changes in media composition [5–7]. Nevertheless, the mechanisms determining the lack of full maturation of hiPSC-CM are poorly understood.

Strong evidence suggests that such cells exhibit temporal changes in phenotype following in vitro differentiation [4,8]. Important aspects of cardiomyocyte maturation, such as the expression of ion channel clusters and the development of functional adrenergic signaling, have been shown to progress towards maturity beyond the first month in culture [9,10]. In contrast to the transcriptomic, electrophysiological and contractile features of hiPSC-CM, there has been limited research on their metabolic profile and the changes accompanying *in vitro* maturation [8,11,12]. This is a critical aspect because metabolic processes are inextricably linked to structural and functional maturation of all cells.

92 In mammalian CM, it is well recognized that pathways involved in energy
93 metabolism undergo profound remodeling during the perinatal period [13]. Anaerobic
94 glycolysis supports the anabolic requirements of the proliferative state during fetal life
95 [14] as well as providing ATP in the relatively hypoxic environment at that stage [15].
96 After birth, there is a switch to oxidative energy production which is thought to also be
97 important for the transition of proliferating immature CM to terminally differentiated
98 cells [16]. The terminal differentiation of CM is accompanied by mitochondrial
99 maturation, with an increase in content, development of a tubular structure with
100 elongated cristae and enhanced polarization [17]. The substrates that are used by CM
101 for energy production vary substantially depending upon the maturation stage. In the
102 fetus, the majority of oxygen consumption is attributable to oxidation of lactate, which
103 is abundantly provided by the placental tissue [18]. After birth, with increased oxygen
104 availability, there is a major shift from anaerobic glycolysis to fatty acid oxidation [19].
105 The metabolic profile of the adult heart is characterized by high flexibility of substrate
106 utilization depending on substrate availability. However, between 50-70% of the ATP
107 in the adult heart is obtained from fatty acid β-oxidation [13].
108 Previous studies have reported that hiPSC-CM have an immature fetal-like
109 metabolic phenotype [2], associated with high rates of glycolysis and very low
110 oxidation potential [20]. However, metabolic changes during prolonged culture have
111 only been characterized at a transcriptomic level [12]. Energy metabolism is tightly
112 intertwined with pathological remodeling in adult cardiomyocytes in conditions such as
113 chronic ischemia and chronic pressure or volume overload [21]. It is therefore
114 important to examine the baseline metabolic profile of hiPSC-CM, if they are to be
115 used to model such pathologies. In this work, we have undertaken a detailed analysis
116 of the metabolic remodeling that occurs in hiPSC-CM with their prolonged culture. We

117 studied the metabolic profile of hiPSC-CM from healthy donors at week 6, commonly
118 employed by many investigators, and after a more prolonged period (12 weeks after
119 CM generation). We used a variety of different readouts to assess anaerobic
120 glycolysis, mitochondrial respiration and network structure, metabolic flux, and
121 expression of key enzymes. We report a roadmap of the metabolic changes that occur
122 in hiPSC-CM during *in vitro* maturation after their initial derivation from hiPSC.

123 **Experimental procedures**

124

125 ***Culture of hiPSC and CM differentiation***

126 The hiPSC lines used in the study, Ctrl1 and Ctrl2, were both derived from
127 healthy donors and were described and characterized previously [22,23]. Cells were
128 maintained in E8 medium on Geltrex®-coated vessels and split every second day by
129 non-enzymatic dissociation (Versene). Cultures were maintained at 37°C, 5% CO_2.
130 CM were differentiated using a protocol of Wnt modulation and metabolic selection as
131 described previously [24], [25]. The differentiation protocol is illustrated schematically
132 in Suppl. Figure 1C-D. hiPSC-CM were cultured in standard maintenance medium
133 (RPMI1640 containing 10 mM glucose and supplemented with B27) [24].

134

135 ***mRNA expression***

136 Total RNA was isolated from cells using the ReliaPrep™ tissue system kit
137 (Promega; Z6012). cDNA was produced from 1 µg of RNA sample using M-MLV
138 reverse transcriptase (Promega; M-1302). Real time qPCR was performed using a
139 QuantiNova SYBR Green kit (Qiagen; 208052) on an ABI StepOne thermocycler.
140 Mean Ct values were normalized using β-2-microglobulin *(B2M)* expression. Primer
141 sequences are reported in Suppl. Table 1.

142

143 ***Immunofluorescence and flow cytometry***

144 For immunostaining, cells were washed with PBS and fixed in formalin-free
145 Histofix® (Roth; P087.1) for 20 minutes at room temperature. Blocking and antibody
146 incubations were performed in 2% w/v BSA, 0.2% v/v Triton™ X-100 in PBS. 3% v/v
147 NGS was added for antibodies raised in goat. Images were captured using an
148 Axiovision Rel4.8-controlled Zeiss inverted fluorescence microscope.

149 For flow cytometry, cells were washed with PBS and incubated with 0.25%
150 trypsin-EDTA until complete detachment. 10% FBS containing medium was added to
151 the cells which were strained through a 22 µm filter. At least $1.5x10^5$ cells per condition
152 were used. Cells were washed with PBS, then fixed in 4% PFA for 20 minutes at room
153 temperature. Incubations with primary antibodies were performed in 0.1% Triton X,
154 1% BSA in PBS, overnight at 4°C. After washing, cells were resuspended in secondary
155 antibody solutions for 45 minutes at room temperature in the dark. After antibodies
156 were washed off via centrifugation, samples were resuspended in PBS, and run
157 through an Accuri C6 flow cytometer. The primary antibodies used are listed in Suppl.
158 Table 2.
159
160 ***Western blotting***
161 Cells were lysed in RIPA-like buffer with protease and phosphatase inhibitors. Total
162 protein was quantified with a Pierce™ BCA assay (Thermo Fisher). Samples were
163 diluted to 1 µg/ml in loading buffer (20% v/v glycerol, 4% w/v SDS, 250 mM Trizma®
164 Base pH 6.8, 1 mM bromophenol blue and 0.5 M 1,4-dithiothreitol). They were boiled
165 at 95°C for 5 minutes. SDS-PAGE was performed using Bolt™ precast gels (Thermo
166 Fisher, NW04120) and MES Buffer. Proteins were transferred onto nitrocellulose
167 blotting membranes. Antibodies were applied overnight at 4°C in TBS-based buffers.
168 Results were acquired using a Licor Odyssey CLx instrument and analyzed using
169 Image Studio Lite software. The antibodies used are listed in Suppl. Table 3. Due to
170 limited availability of protein samples from long-term cultures of hiPSC-CM, western
171 blots membranes were cut and probed with multiple antibodies. Sometimes
172 membranes were stripped and re-blotted. As a result, multiple targets may have the
173 same loading control. Whilst only one representative loading control is shown per

174 figure, quantification of each target was performed using its own appropriate loading
175 control.
176
177 ***Extracellular flux analysis***
178 Studies were performed using a Seahorse xF24 analyzer. Cells were plated on
179 Geltrex®-coated 24-well microplates at $5x10^4$ cells/well, 1 week before the assay.
180 Cartridges were hydrated following the manufacturer's instructions. Media were
181 prepared on the day of each experiment, using a DMEM basal medium without
182 glucose, glutamine or phenol red. Appropriate substrates were added as described for
183 each assay (10 mM D-glucose, 2 mM sodium-pyruvate, 4 mM sodium-lactate) and
184 media were brought to pH 7.4 at 37°C. Cells were equilibrated in assay medium for
185 45 minutes before the experiment. Three distinct assays were performed (Table 1)
186 and the following drugs were employed: a complex V inhibitor, oligomycin (Sigma,
187 75351); a mitochondrial pyruvate carrier (MPC) inhibitor, UK5099 (Sigma, PZ0160); a
188 glutaminase inhibitor, Bis-2-(5-phenylacetamido-1,3,4-thiadiazol-2-yl)ethyl sulfide
189 (BPTES) (Sigma, SML0601); an irreversible O-Carnitine palmitoyltransferase-1
190 (CPT1) inhibitor, Etomoxir (Sigma, E1905); the protonophore, Carbonyl cyanide 4-
191 (trifluoromethoxy)phenylhydrazone (FCCP) (Sigma, C2920); a complex III inhibitor,
192 antimycin A (Sigma, A8674); a complex I inhibitor, rotenone (Sigma, R8875). For
193 assays involving fatty acid oxidation, cells were starved overnight in a medium
194 containing 2 mM L-glutamine and supplemented with 0.5 mM D-glucose and 0.5 mM
195 L-carnitine hydrochloride. 1 mM BSA-conjugated palmitate was added to the assay
196 medium immediately before the assay and the FCCP concentration was raised to 1
197 μM.
198

	Glycolysis stress test		Mitochondrial Stress test		Fuel Source test	
Medium	Substrate free		Single-substrate		Complete	
Injection 1	Glucose	10 mM	Oligomycin A	1 μM	UK5099 or BPTES or Etomoxir	7.5 μM 10 μM 15 μM
Injection 2	Oligomycin A	1 μM	FCCP	0.5 μM	Combination	
Injection 3	2-Deoxy-D-Glucose	100 mM	Antimycin A + Rotenone	1 μM 1 μM	Antimycin A + Rotenone	1 μM 1 μM

Table 1. Summary of protocols for Seahorse analyzer

In some experiments, cells were fixed using 4% PFA for 15 minutes after completion of assays in order to perform cell-number normalization. They were then treated with 2 μg/ml DAPI for 10-15 minutes to visualize nuclei. UV-fluorescence nuclear counting was automated on an Olympus IX81 microscope and used as an index of cell number for data normalization.

^{1}H-^{13}C-nuclear magnetic resonance (NMR) to estimate metabolic flux

We performed some studies using uniformly ^{13}C-labeled glucose (^{13}C-U glucose) and NMR to estimate the activity of different glucose-utilizing pathways in hiPSC-CM [26]. Cells (>5x10^{6} cells per sample) were incubated with ^{13}C-U glucose (10 mM) for 16 hours. Cells were kept on dry ice and scraped in methanol. Chloroform and water were added and the polar phase was isolated after cold centrifugation. Samples were dried and subsequently reconstituted in P-buffer (40 mM NaH_2PO_4, 60 mM Na_2HPO_4, 0.01 % w/v DSS, 1.5 mM Imidazole, in D_2O). They were analyzed at 25 ^{o}C on a Bruker Avance 700 MHz NMR spectrometer. The ^{13}C labeled metabolites were calculated using heteronuclear single quantum coherence (HSQC) as described previously [26]. Spectra were processed using the MetaboLab software package [27].

219

220 ***Mass spectrometry-based metabolomics***

221 $5x10^5$ cells/well were seeded in 6-well plates one week before the harvesting.
222 Cells were washed with ice-cold PBS and quenched with ice-cold methanol and water
223 (v/v 1/1). Subsequently, the multi-well plate was put on ice and metabolites were
224 extracted as previously described [28]. Briefly, cells were scraped in extraction
225 solvents, transferred to a tube containing an equal volume of chloroform and agitated
226 in a shaker for 20 minutes at 1400 rpm 4 °C, followed by centrifugation (5 minutes,
227 16,000x g, 4°C) to obtain the upper polar metabolite phase and protein interphase.
228 The polar phase was transferred to a fresh tube and dried in a speed-vac. The protein
229 interphase was washed with methanol and then reconstituted in RIPA buffer with
230 protease and phosphatase inhibitors. Total protein was quantified with a Pierce™ BCA
231 assay (Thermo Fisher) and used as sample normalization technique.

232 The dried polar metabolite fractions were reconstituted in acetonitrile/water (v/v 3/2)
233 and analyzed using a 1290 Infinity II ultrahigh performance liquid chromatography
234 (UHPLC) system coupled to a 6546 quadrupole time-of-flight (Q-TOF) mass
235 spectrometer (Agilent Technologies). Samples were separated on a Poroshell 120
236 HILIC-Z column (2.1 × 100 mm, 2.7 µm) and analyzed in negative ionization mode
237 using water with 10 mM ammonium acetate (solvent A) and acetonitrile with 10 mM
238 ammonium acetate (solvent B), both solvents containing 5 µM InfinityLab deactivator
239 additive (Agilent Technologies). The elution gradient used was as follows: isocratic
240 step at 95% B for 2 minutes, 95% to 65% B in 12 minutes, maintained at 65% B for 3
241 minutes, then returned to initial conditions over 1 minute, and then the column was
242 equilibrated at initial conditions for 8 minutes. The flow rate was 0.25 mL/min; injection
243 volume was 5 µL, and the column oven was maintained at 30 °C. The 6546 Q-TOF
244 was operated at 2 GHz extended dynamic range with a mass acquisition range from

245 0-1700 m/z. The drying and sheath gas temperature was set at 250°C and 380 °C,
246 respectively, with the nebulizer pressure at 45 psi and voltage 3000. The fragmentor
247 voltage was set at 115 V. Feature annotation and metabolite identification was
248 performed with MassHunter Profinder (version 10.0.2, Agilent Technologies) using our
249 in-house curated metabolite library based on metabolite standards. Metabolite levels
250 are represented as ion peak height normalized to protein concentration. Data
251 visualization and statistical analyses were performed using MetaboAnalyst v5.0 [29].
252
253 ***Mitochondrial parameters***
254 To calculate the mitochondrial fraction in live cells, they were loaded with
255 MitoTracker® Green (1:1000 in culture medium for 30 minutes). Cells were then
256 imaged by epifluorescence and the mitochondrial fraction reported as signal area/total
257 cell area. Further live cell imaging using MitoTracker® green was conducted on a
258 Nikon A1R spinning disc confocal microscope. Z-stacks were acquired and images
259 were analyzed using the MiNa ImageJ macro tool by the Stuart lab [30].
260 Mitochondrial DNA (mtDNA) content was normalized to nuclear DNA (nDNA).
261 nDNA was obtained via qPCR on genomic DNA isolated from cells harvested in 100
262 mM Tris-HCl, pH 8; 5 mM EDTA, pH 8; 0.2 % w/v SDS; 200 nM NaCl. *B2M* was used
263 as nuclear DNA reference. Primers for mtUUR were: forward,
264 CACCCAAGAACAGGGTTTGT; reverse, TGGCCATGGGTATGTTGTTA.
265 Mitochondrial membrane potential was assessed using FACS in cells loaded
266 with tetramethylrhodamine ethyl ester (TMRE) for 30 minutes in culture medium [31].
267 Mitochondrial calcium levels were estimated using cells transfected with a
268 mitochondrial-targeted Cameleon FRET probe as previously described [31]. FRET
269 measurements were performed on a Nikon A1R confocal microscope.
270

271 ***Transmission electron microscopy***

272 Cells grown on Thermonox coverslips were fixed in 2% glutaraldehyde in 0.1 M
273 sodium cacodylate buffer, pH 7-7.4, for 60 minutes (room temperature) followed by a
274 post-fixation step with 1% osmium tetroxide in 0.1 M sodium cacodylate buffer for 1
275 hour (room temperature). Following fixation the cells were dehydrated in a graded
276 series of ethanol, equilibrated with propylene oxide, and infiltrated with epoxy resin
277 (Agar100 from Agar Scientific) using gelatin molds and cured at 60°C for 48 hours.
278 Coverslips were removed from the resin blocks using liquid nitrogen and 70-80 nm
279 ultrathin sections were prepared with an Ultracut E ultramicrotome (Reichert-Jung,
280 Leica Microsystems Ltd, Milton Keynes, UK), mounted on copper grids, and
281 contrasted with uranyl acetate and lead citrate. Samples were examined on a JOEL
282 JEM 1400Plus Transmission Electron Microscope operated at 120 kV, and images
283 acquired with a high sensitivity sCMOS camera at the JEOL Centre for Ultrastructural
284 Imaging (CUI).

285

286 ***Statistical analysis***

287 Data are expressed as mean ± SD or S.E.M. as indicated. Statistical analyses
288 were performed using GraphPad Prism 7. Samples distributions were tested for
289 normality using the Shapiro-Wilk test. Unpaired two-tailed Student's t-test or Mann-
290 Whitney test were then applied as appropriate. Groups were compared by 1-way or 2-
291 way analyses of variance (ANOVA) as appropriate followed by Tukey's multiple
292 comparisons tests, or non-parametric Kruskal-Wallis followed by Dunn correction
293 when samples distributions were not normal. $p<0.05$ was considered as the threshold
294 for statistical significance.

295

296 **Results**

297

298 ***Prolonged culture aids structural maturation of hiPSC-CM.***

299 We used control hiPSC cell lines from two independent healthy donors, Ctrl1
300 and Ctrl2, which were previously described [22,23]. Both demonstrated features of
301 stemness and pluripotency as assessed by typical morphology, alkaline phosphatase
302 (ALP) activity and the expression of the self-renewal markers NANOG, SOX2, LIN28,
303 TRA-1-60 and SSEA-4 assessed by immunofluorescence (Supplementary Fig. 1A-B).
304 The differentiation into hiPSC-CM [32] was accompanied by the repression of
305 pluripotency and self-renewal genes (*NANOG, PUO5F1, LIN28, SOX2*), followed by
306 an early transient increase of stage-specific early cardiogenic factor *GATA4* and a
307 significant increase in expression of the cardiac-specific markers *ACTN2* and *MY2*
308 (Supplementary Fig. 1C-F). By week 6 of hiPSC-CM culture, there was complete
309 suppression of pluripotency markers while the CM purity as assessed by the
310 percentage of α-actinin positive (α-Actinin^{+}) cells by flow cytometry was >95% (Fig.
311 1A). The percentage of cells positive for α-actinin, ventricular myosin light chain 2
312 (MLC2v) and cardiac troponin T (cTnT) was similar at week 6 and after prolonged
313 culture to week 12. We observed a substantial increase in the intensity of α-actinin
314 and MLC2v fluorescence between 6 weeks and 12 weeks, indicative of ongoing CM
315 maturation throughout this period (Fig. 1A). These results are consistent with previous
316 reports [33,34]. Sarcomere structure as assessed by co-staining cells with antibodies
317 against C-terminal or N-terminal portions of titin (markers of the M-line and Z-disk,
318 respectively) and α-actinin (Z-disk) was similar in differentiated hiPSC-CM at week 6
319 and in cells cultured for 12 weeks, with a striated pattern of localization of these
320 myofilament proteins (Fig. 1B-C). However, sarcomere regularity was enhanced in
321 cells at week 12 compared to matched counterparts at week 6 (Fig. 1C).

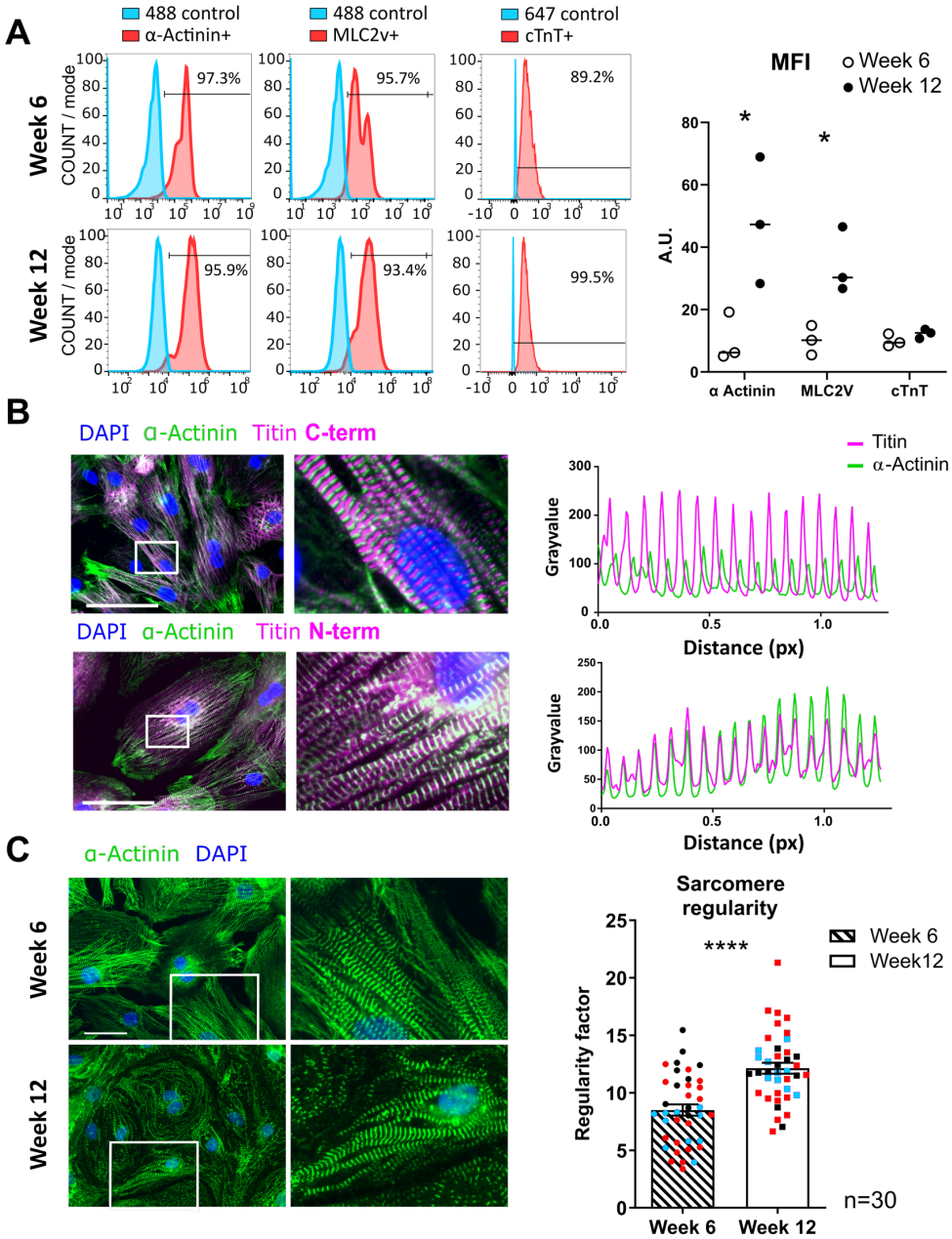

Figure 1. Effect of prolonged culture of hiPSC-CM on sarcomere protein levels and ultrastructure. A) FACS analysis of hiPSC-CM at week 6 and week 12. Left panel: positive cells in the cell population (%); right panel: mean fluorescence intensity (MFI). *, $p<0.05$ by unpaired t-tests; n=3 independent differentiation experiments. B) Left panel: Representative immunofluorescence images of hiPSC-CM at week 6 for the markers indicated; scale bar, 200 µm. Right panel: co-localization patterns of immunofluorescence. The Pearson correlation coefficients were: Titin C-term (C-terminal) and α-Actinin, week 6 r=-0.360, week 12 r=-0.448; Titin N-term and α-Actinin, week 6 r=0.861, week 12 r=0.853. n of pairs=189. Results were replicated in 3 independent differentiation experiments for both time points. C) Left panel: representative α-Actinin immunofluorescence micrographs. Right panel: quantification of sarcomere regularity from immunofluorescence images processed via Fast Fourier Transformation. Data ± S.E.M. ****, $p<0.0001$ by unpaired t-tests after normal distribution was confirmed via Shapiro-Wilk test. n=30 cells from 3 independent differentiation experiments, indicated by colors, >10 cells/experiment.

338

339 ***Restructuring of the glycolytic network.***

340 Fetal CM are thought to be highly reliant on anaerobic glycolysis for energy
341 production but enzymatic and topological restructuring of the glycolytic network is
342 reported to be necessary for the differentiation and maturation of CM towards oxidative
343 energy metabolism [35]. We compared features of glycolysis and related pathways in
344 hiPSC-CMs cultured in standard RPMI1640 containing 10 mM glucose and
345 supplemented with B27 for 6 week or 12 weeks. The quantification of extracellular
346 acidification rate (ECAR) on a Seahorse flux analyzer, as an index of lactate
347 production, showed no differences between the two stages (Fig. 2A). There was also
348 no difference in the glycolytic reserve between 6 and 12 weeks, as assessed by a
349 glycolytic stress test in which complex V (ATP synthase) is inhibited with oligomycin
350 (Fig. 2A).

351 We further characterized expression of enzymes involved in glucose uptake
352 and utilization. The protein levels of the glucose transporters, GLUT1 (SLC2A1) and
353 GLUT4 (SLC2A4), were similar in week 6 and week 12 cells. However, levels of the
354 lactate transporter MCT4 (SLC16A3) were 4-fold higher in week 12 compared to week
355 6 hiPSC-CM (Fig. 2B). We assessed the protein levels of a panel of enzymes involved
356 in glycolysis (Fig. 2C). Interestingly, week 12 hiPSC-CM showed a significant isoform
357 shift from hexokinase 2 (HK2) to hexokinase 1 (HK1), and an increase in muscle
358 phosphofructokinase (PFKM). No significant changes were observed in the other main
359 glycolytic pathway enzymes. Hexokinase and PFKM are proximal rate-limiting
360 enzymes in the glycolytic pathway, which influence the partitioning of glycolytic
361 intermediates between forward glycolysis and entry into the tricarboxylic acid (TCA)
362 cycle or other glycolytic branch pathways.

363

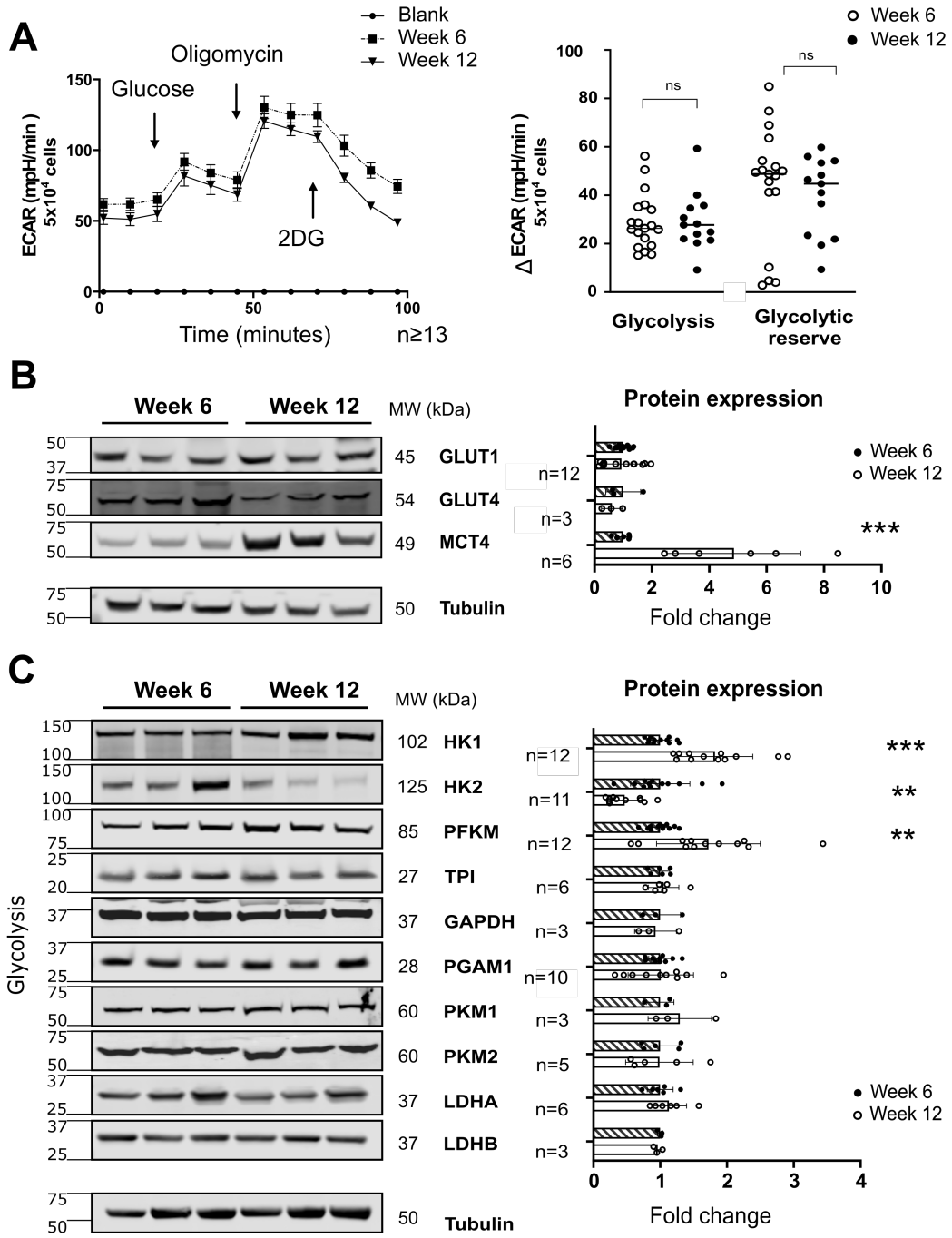

Figure 2. The glycolytic network in maturing hiPSC-CM. A) Glycolysis stress tests in week 6 versus week 12 hiPSC-CM, performed on a Seahorse analyzer. Left panel: Average profiles of the extracellular acidification rate (ECAR), n≥13 profiles per condition, from 4 independent differentiations. 2DG: 2-deoxyglucose. Right panel: Quantification of glycolytic parameters. n≥13 wells per condition from 4 independent differentiation experiments run on 4 separate Seahorse plates B) Left panel: Representative western blots for carbohydrate plasma membrane facilitated transporters. Right panel: Quantification of relative protein expression. C) Left panel: Representative western blots for glycolytic enzymes. Right panel: Quantification of relative protein expression. All data are mean ± S.D. **, p<0.01; ***, p<0.001; ****, p<0.0001 by unpaired t-tests (if normal distribution was confirmed via Shapiro-Wilk

test) or non-parametric Mann-Whitley test. 3⩽n⩽12 differentiation experiments as indicated in the figure. GLUT: glucose transporter; MCT4: monocarboxylate transporter 4; HK: hexokinase; PFKM: muscle phosphofructokinase; TPI: triosephosphate isomerase; GAPDH: glyceraldehyde-3-phosphate dehydrogenase; PGAM: 2,3-bisphosphoglycerate-independent phosphoglycerate mutase; PKM: pyruvate kinase Muscle isoform; LDHA and LDHB: lactate dehydrogenase subunit A and B.

Turning to the entry of glycolytic intermediates into the TCA cycle, the expression of the pyruvate dehydrogenase alpha subunit (PDHαE1), which catalyzes the irreversible entry of pyruvate into the TCA cycle, was 2-fold higher in week 12 hiPSC-CM whereas its inhibitory phosphorylation at S293 (site1) [36] seemed lower, although not statistically significant (Fig. 3A). In week 12 hiPSC-CM we also observed a conspicuous isoform switch between pyruvate dehydrogenase kinase-1 (PDK1) and pyruvate dehydrogenase kinase-4 (PDK4) which increased 15-fold and a smaller increase in pyruvate dehydrogenase phosphatase-1 (PDP1) (Fig. 3B). Protein levels of pyruvate carboxylase (PC), which may support anaplerotic entry of intermediates into the TCA cycle, were similar in cells at both stages (Fig. 3A).

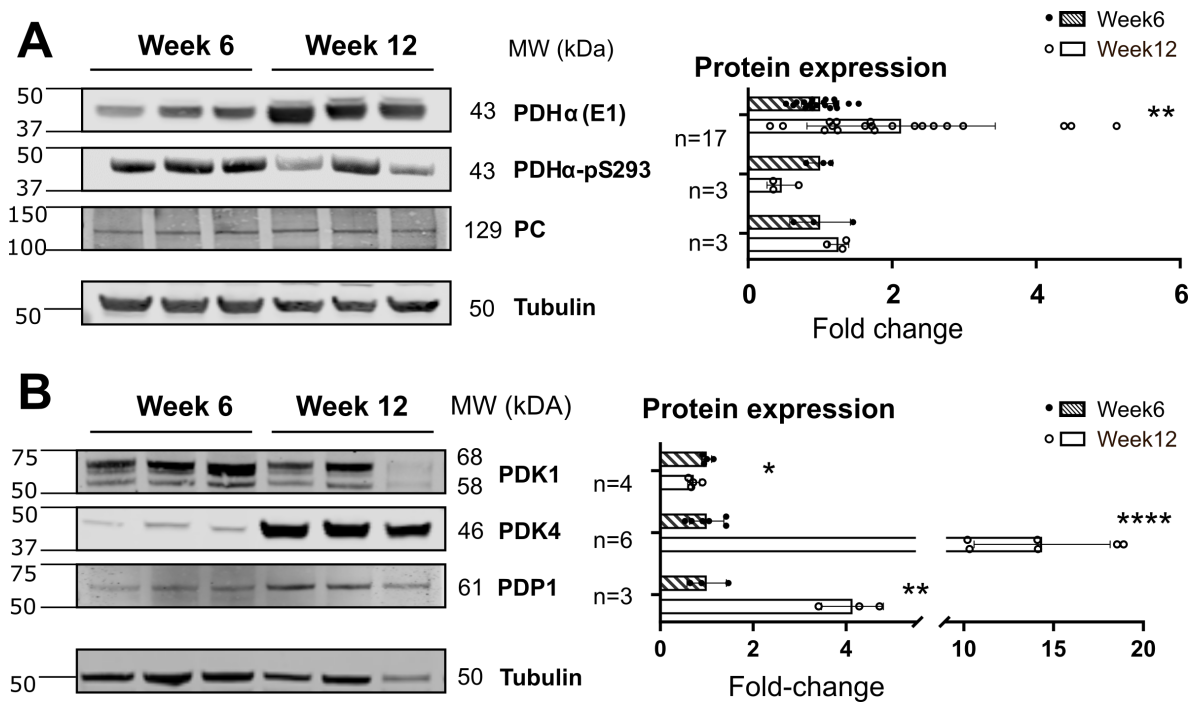

397 **Figure 3. Changes in protein levels of enzymes involved in flux into the TCA**. A-
398 B) Left panels are representative western blots for the proteins shown. Right panels
399 show quantification of relative protein expression as fold-change compared to week 6.
400 Data are mean ± S.D. *, $p<0.05$; **, $p<0.01$; ****, $p<0.0001$ by unpaired t-test (if normal
401 distributions were confirmed by Shapiro-Wilk test) or non-parametric Mann-Whitney
402 test. $3 \leqslant n \leqslant 17$ differentiation experiments as indicated in figure. PDH: pyruvate
403 dehydrogenase; PC: pyruvate carboxylase; PDK, pyruvate dehydrogenase kinase.
404

405 Flux through anaerobic glycolysis was also assessed by the ^{13}C enrichment of
406 [1,2,3]-^{13}C lactate in cells incubated with U-^{13}C glucose, via NMR analysis. This was
407 found similar in week 6 and week 12 hiPSC-CM (Fig. 4A). Flux into the pentose
408 phosphate pathway (PPP) was assessed by measuring [2,3]^{13}C lactate isotopomer.
409 This analysis relies on the re-entry of differently labelled glyceraldehyde-3-phosphate,
410 produced from PPP-derived fructose-6-phosphate via transketolase, back into
411 glycolysis and the subsequent generation of lactate [37]. (Fig. 4A). The estimated PPP
412 flux was found to be similar in week 6 and week 12 hiPSC-CM. However, the protein
413 levels of the two major PPP regulatory enzymes, glucose 6-phosphate dehydrogenase
414 (G6PD) and 6-phosphogluconate dehydrogenase (PGD), were significantly lower at
415 week 12 compared to week 6 hiPSC-CM (Fig. 4B). The hexosamine biosynthetic
416 pathway (HBP), another glycolytic branch pathway, results in the formation of uridine
417 diphosphate-N-acetylglucosamine (UDP-GlcNAc) which is used in post-translational
418 O-GlcNAcylation of proteins [38]. When analyzing the levels of the rate-limiting HBP
419 enzymes, we observed a relative change in glutamine-fructose-6-phosphate
420 aminotransferase (GFAT) isoforms, from GFAT2 to GFAT1, with a significant
421 reduction in GFAT2 in week 12 hiPSC-CM (Fig. 4B). While expression of O-GlcNAc
422 transferase (OGT) was readily detectable a both stages, levels of O-GlcNAcase
423 (OGA) were low in both conditions (Fig. 4B). The level of overall protein O-
424 GlcNAcylation was not significantly different between week 6 and week 12 hiPSC-CM
425 (Fig. 4C).

426 Collectively these data suggest a sustained flux through the glycolytic pathway
427 which, in week 12 hiPSC-CM, seems preferentially directed towards TCA cycle entry,
428 rather than anaerobic or glycolytic branch pathways.

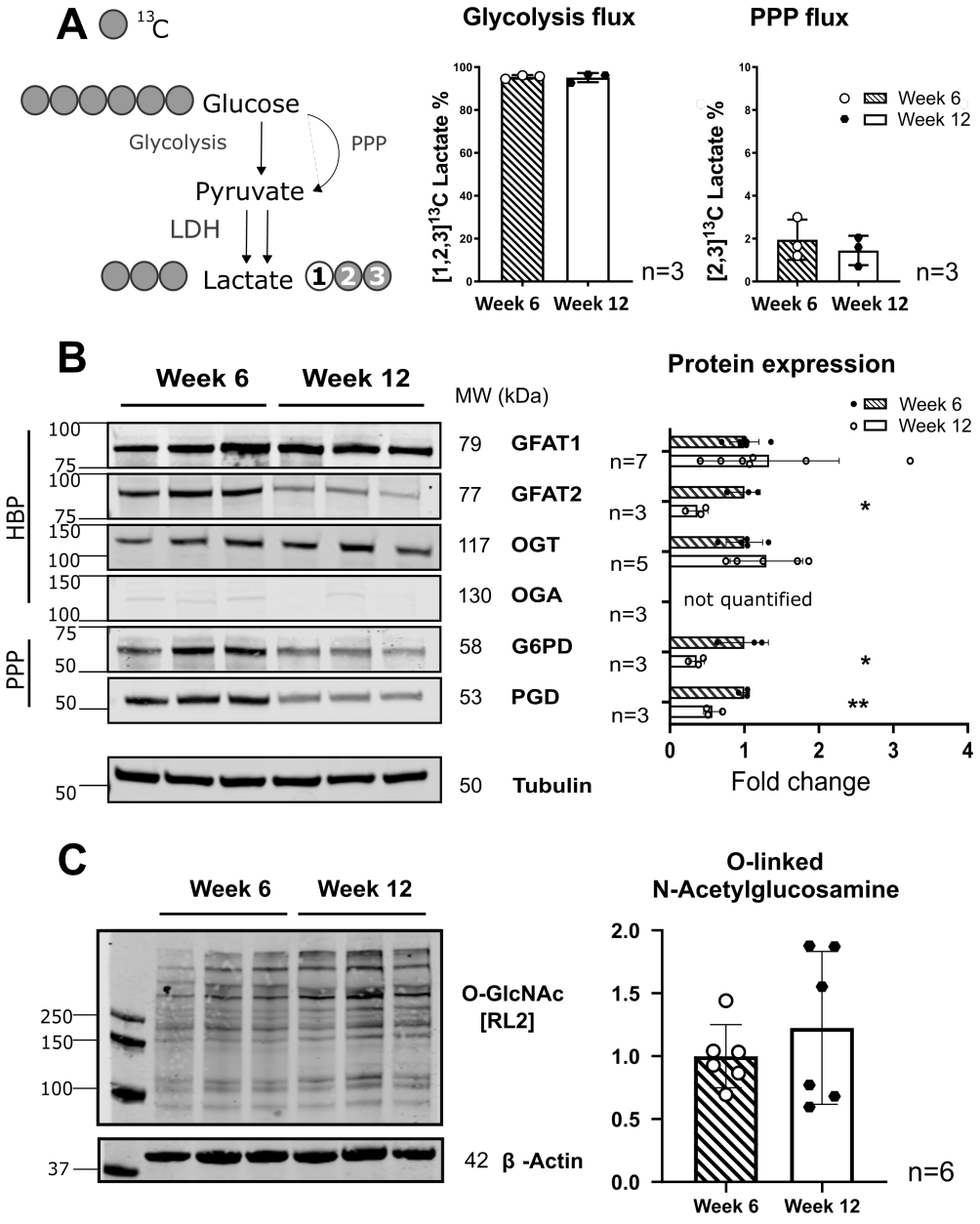

429

430 **Figure 4. Characterization of glycolytic branch pathways.** A) Left: Schematic
431 representation of lactate labeling patterns after metabolism of U-^{13}C glucose through
432 the glycolytic or pentose phosphate pathway (PPP). Right: Quantification of the % ^{13}C
433 labeling of [1,2,3]^{13}C-lactate and [2,3]^{13}C-lactate to estimate glycolytic flux and PPP
434 flux respectively. Cells were incubated in 10 mM U-^{13}C Glucose for 16 h. Metabolite
435 quantification was undertaken by HSQC NMR spectroscopy. Data are mean ± S.D.;
436 n=3 independent differentiations. B) Left panels: Representative western blots for the
437 targets shown. Right panels: Quantification of relative protein expression; data are
438 mean ± S.D. *, $p<0.05$; **, $p<0.01$ by unpaired t-tests (normal distributions were

assessed via Shapiro-Wilk test). $3 \leqslant n \leqslant 7$ independent differentiations as indicated in figure. C) Left panel: Representative western blot targeting O-linked N-Acetylglucosamine. Right panels: Quantification of relative expression; data are mean ± S.D. $p>0.05$ by unpaired t-test (normal distributions were assessed via Shapiro-Wilk test). n=6 independent differentiations. PPP: pentose phosphate pathway; GFAT: glutamine - fructose-6-phosphate transaminase; OGT: O-linked N-acetylglucosamine (GlcNAc) transferase; OGA: protein OGlcNacase; G6PD: glucose-6-phosphate dehydrogenase; PGD: phosphogluconate dehydrogenase.

These observations were corroborated by targeted metabolomics analysis by LC-MS of polar extracts from hiPSC-CM cultured in 10 mM glucose. Principal Component Analysis (PCA) convincingly differentiated between hiPSC-CM at week 6 and week 12 (Fig. 5A). Metabolites that were significantly different by >1.5 fold between time-points are represented in Figure 5B. Figure 5C shows hierarchical clustering of the 50 metabolites that showed the most pronounced differences between week 6 and week 12 hiPSC-CMs. Generally, proximal glycolytic intermediates (e.g. G6P, F6P, FBP, 1,3BPG) were more abundant in cells at week 6, while pyruvate and TCA cycle precursors such as 2-hydroxyglutarate and D-isocitrate, were more represented in 12 weeks samples. An Over Representation Analysis (ORA) using FDR correction, highlighted anaerobic glycolysis and gluconeogenesis as the most enriched pathways in differentiated hiPSC-CMs at week 6 compared to week 12 (Suppl. Fig. 2A).

It is noteworthy that UDP-GlcNAc abundance was significantly lower in hiPS-CM at week 12. Together with the reduced GFAT2 expression shown above, this is consistent with a reduced flux through the HBP, and suggests a redirection of flux away from this glycolytic branch pathway.

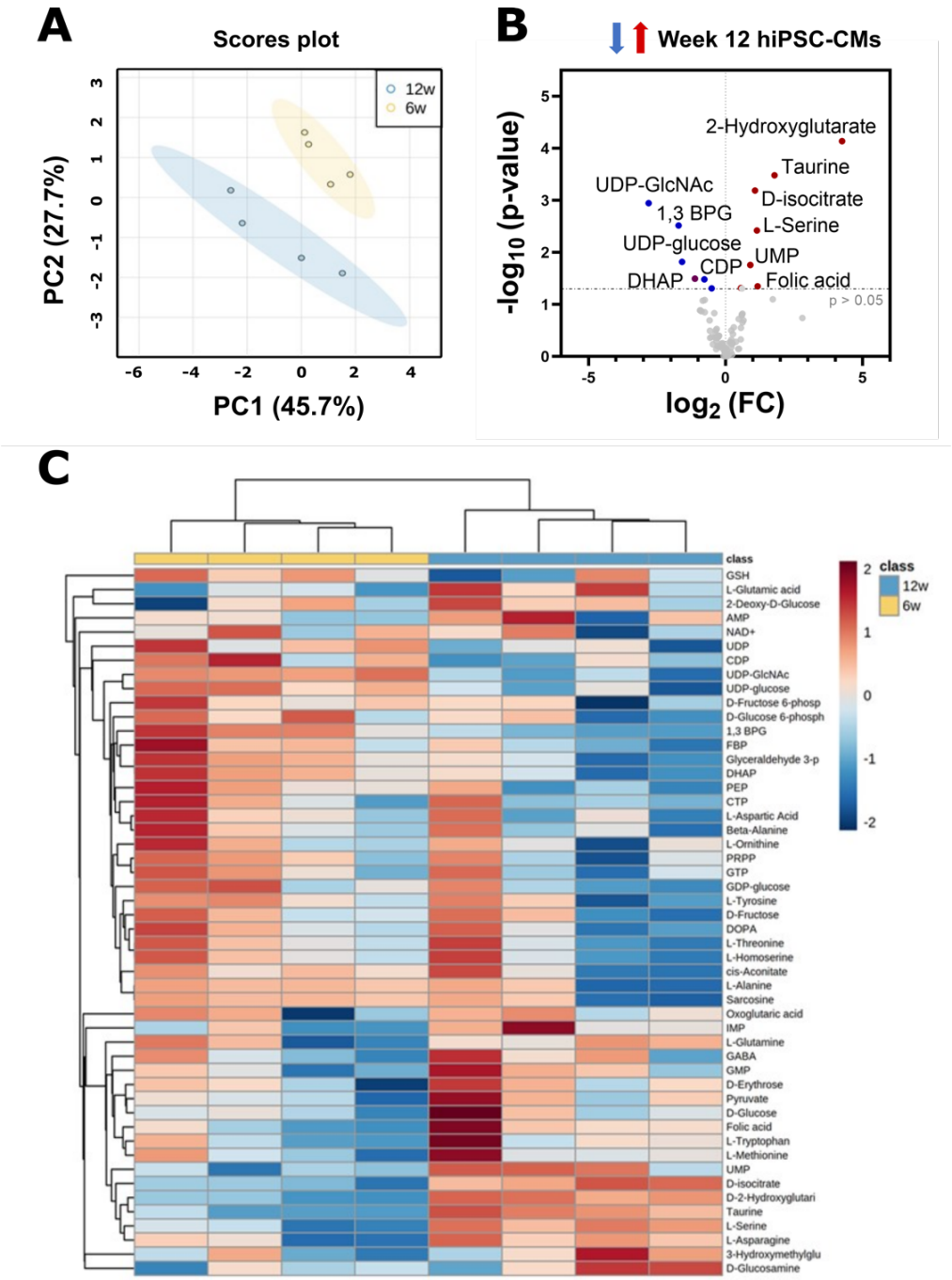

Figure 5. Targeted metabolomics of polar metabolites in week 6 versus week 12 hiPSC-CM. A) Principal Component Analysis (PCA) based on metabolite abundance measured as ion peak intensities detected by LC-MS. The explained variances of each principal component (PC) are shown in brackets. B) Volcano plot comparing metabolite levels between hiPSC-CM at week 6 and week 12. Statistical significance was assessed by unpaired t-tests. Metabolites meeting a threshold of fold-change >1.5 and $p<0.05$ were considered as statistically significant. Blue: decreased, red: increased, in 12 week hiPSC-CM. C) Hierarchical clustering shown as heat map highlighting the 50 metabolites with the most pronounced differences in abundance between hiPSC-CM at week 6 and week 12. Ion peak intensities were $\log_{10}$ transformed, mean centred and normalized to protein concentration of each sample. n=4 independent differentiation experiments**.**

479 ***Oxidative metabolism and substrate preference.***

480 To assess the relative balance between anaerobic glycolysis and oxidative
481 metabolism, hiPSC-CM were incubated for 1 hour in RPMI 1640 medium
482 supplemented with glucose, fatty acids (BSA-conjugated palmitate), L-carnitine and
483 glutamine, in order to provide cells with a choice of different oxidation substrates. The
484 oxygen consumption rate (OCR) and ECAR were quantified simultaneously on a
485 Seahorse instrument. This revealed that the OCR/ECAR ratio was significantly higher
486 in cells at week 12 compared to week 6 (Fig. 6A), indicating a time-dependent shift
487 towards a more oxidative metabolic profile in the presence of multiple oxidation
488 substrates.

489 Next, we evaluated the relative contribution of each substrate to total oxidative
490 metabolism. In cells incubated in complete medium (as above), OCR was measured
491 in the presence of specific inhibitors, each targeting the mitochondrial intake of a single
492 substrate. We used etomoxir to inhibit CPT1 and therefore fatty acid import and
493 oxidation, BPTES to inhibit glutaminase, and UK5099 to inhibit the mitochondrial
494 pyruvate carrier and therefore glucose oxidation. We quantified the corresponding
495 reductions in OCR (Fig. 6B). A single inhibitor was added in step 1, then the other two
496 inhibitors combined in step 2, and finally Antimycin A and rotenone in step 3 to
497 completely inhibit the electron transport chain (ETC). Different substrate inhibitor
498 combinations were added in different wells but with all the assays performed on a
499 single plate. Using this approach, we calculated the proportion of total OCR that was
500 accounted for by each substrate provided in the complete medium. This analysis
501 revealed that the relative contribution of fatty acid oxidation to total OCR increased
502 significantly at week 12 compared to week 6 hiPSC-CM, at the expense of glucose

503 oxidation (Fig. 6B). A significant amount of glutamine oxidation contributed to the
504 overall OCR, similarly at both stages.

505 The relative increase in fatty acid oxidation was accompanied by a significant
506 increase in levels of PPARα, the master transcription factor that drives lipid
507 metabolism [39], in week 12 compared to week 6 cells (Fig. 6C). We also observed
508 increased levels of the plasma membrane fatty acid transporter CD36 and the
509 mitochondrial β-oxidation enzymes medium-chain acyl-CoA dehydrogenase
510 (ACADM) and 3-hydroxyacyl-CoA dehydrogenase (HADH), in long-term cultured cells
511 (Fig. 6C). The levels of carnitine-palmitoyl transferase 1 (CPT1a) were similar in
512 differentiated and long-term cultured cells. Since CPT1 is sensitive to inhibition by
513 malonyl-CoA, we quantified the levels of acetyl-CoA carboxylase (ACC1 and 2) and
514 malonyl-CoA decarboxylase, which regulate malonyl-CoA levels [40]. Total ACC2
515 increased at week 12 compared to week 6 hiPSC-CM but there were no differences
516 in ACC1 or malonyl-CoA decarboxylase (Fig. 6D). However, a shift in ACC1
517 electrophoretic mobility in late-stage hiPSC-CM samples might indicate differences in
518 post-translational modification. Western blot analysis of phosphorylation at S79 (an
519 AMPK-specific site) could not distinguish between isoforms and showed very low
520 phosphorylation levels in comparison to other cardiac cell lines (data not shown).

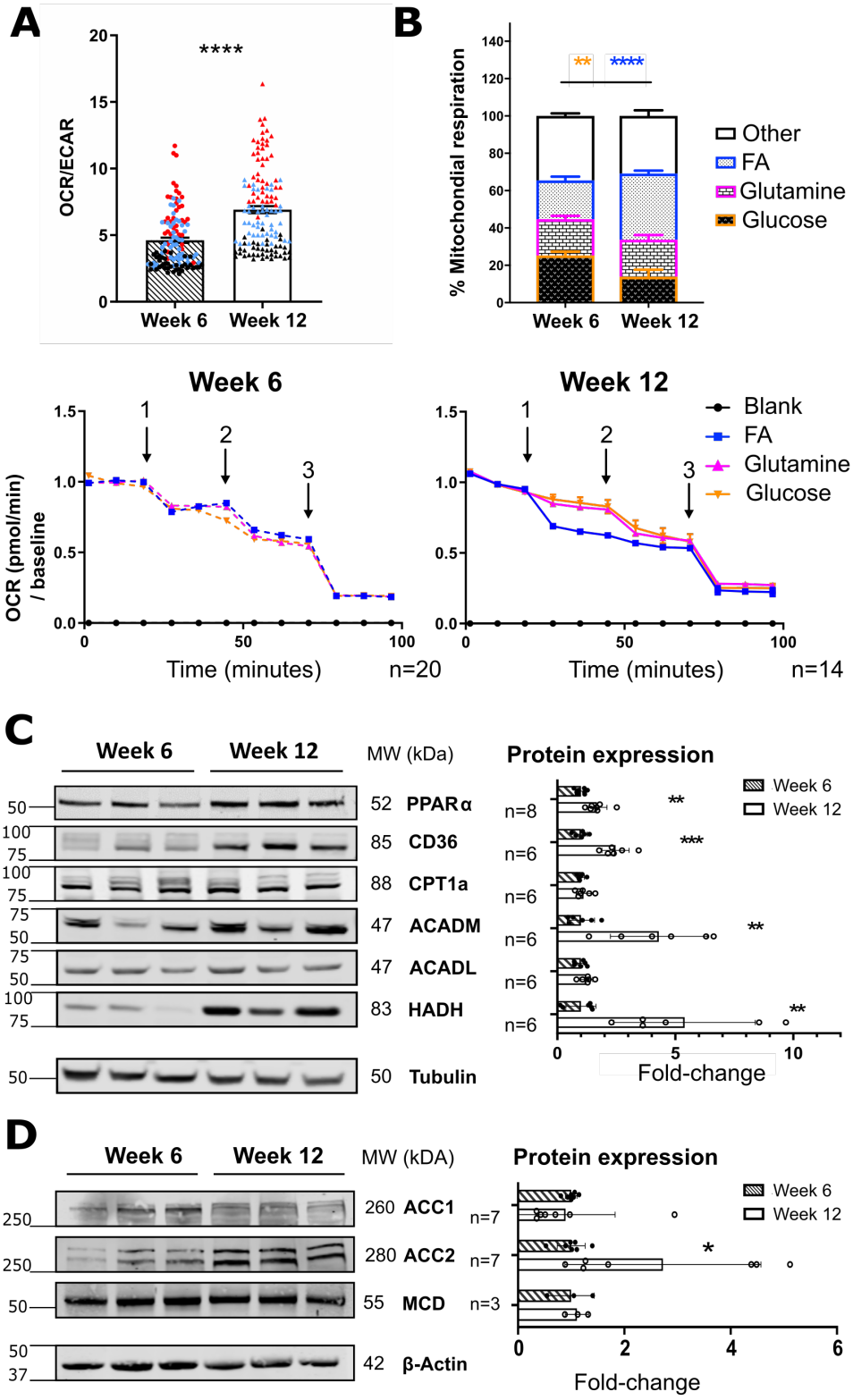

Figure 6. Relative anaerobic versus oxidative metabolism and alterations in substrate utilization in hiPSC-CM. A) Ratio of oxygen consumption rate (OCR) over extracellular acidification rate (ECAR) in week 6 versus week 12 hiPSC-CM equilibrated in complete medium. Data are mean ± S.E.M. ****, p<0.0001 by Mann-Whitney test. n>110 wells per time-point from 3 independent differentiation experiments represented by colors, run on 6 separate plates. B) Bottom panels: In

528 Fuel Source tests, the utilization of each substrate was targeted by a pharmacological
529 inhibitor. The substrates were fatty acids (FA), glutamine and glucose. A single
530 inhibitor was added at time-point 1; the other two inhibitors were added at time-point
531 2 (all combinations were performed in parallel on the same plate); and Antimycin A
532 and Rotenone were added at time-point 3 (assay summary in Table 1). The graphs
533 show the average profiles of OCR, week 6, n= 20 profiles; week 12, n= 14 profiles,
534 from 3 independent differentiations, run on 6 separate plates. B) Top right panel:
535 quantification of the contribution of different substrates to total OCR. Data are mean ±
536 S.E.M. **, $p<0.01$ and ****, $p<0.0001$ by 2 way ANOVA followed by Tukey's test after
537 normal distributions were confirmed via Kolmogorov-Smirnov normality test. n=20
538 (week 6); n=14 (week 12), from 3 independent differentiation experiments run on 6
539 separate plates. The colors of the asterisks indicate the substrate being considered
540 for week 6 vs week 12 comparison. C-D) Left panel: Representative western blots for
541 targets involved in FA metabolism. Right panel: Quantification of relative protein
542 expression. Data are mean ± S.D. **, $p<0.01$; ***, $p<0.001$; by unpaired t-tests (if
543 normal distribution was confirmed via Shapiro-Wilk test) or non-parametric Mann-
544 Whitley test. $3 \leqslant n \leqslant 8$ as indicated in figure. PPARα: peroxisome proliferator activated
545 receptor alpha; CD36: cluster of differentiation, molecule 36; CPT1a: carnitine-
546 palmitoyl transferase subunit 1a; ACADM/L: medium/light chain acyl-CoA
547 dehydrogenase; HADH: hydroxyacyl-CoA dehydrogenase; ACC, acetyl-CoA
548 carboxylase; MCD, malonyl-CoA decarboxylase.
549

550 ***Mitochondrial function, structure and content.***

551 Changes in mitochondrial structure and function are key drivers of metabolic
552 maturation in the developing heart [16,17]. We therefore compared mitochondrial
553 parameters between week 6 and week 12 hiPSC-CM.

554 To assess mitochondrial oxidative function, we measured the basal and
555 maximal mitochondrial respiration at week 6 versus week 12 hiPSC-CM when
556 individual substrates were provided, one at a time (pyruvate, glucose, lactate or BSA-
557 palmitate), using mitochondrial stress tests (Fig. 7A). No significant differences were
558 detected between time-points in proton leak or non-mitochondrial oxygen consumption
559 (quantifications not shown). Also, similar levels of oxidative energy metabolism, as
560 indicated by the ATP-linked OCR (quantifications not shown), were observed,
561 denoting similar energy requirements in culture. However, week 12 hiPSC-CM were
562 characterized by markedly higher respiratory reserve compared to week 6 cells - an
563 index of the cell capability to meet increased energy demands, often used as an

564 indication of cell fitness - for each of the carbon sources tested, suggesting a potential
565 increase in mitochondrial maturation (Fig. 7A).
566 To test if these results are consistent with other features of mitochondrial maturation,
567 we compared the mitochondrial membrane potential ($\Delta\Psi_{mt}$) between time-points,
568 using the cationic fluorescent dye TMRE, and found it to be significantly higher at week
569 12 (Fig. 7B). In addition, the basal mitochondrial calcium levels, quantified using a
570 mitochondrial-targeted FRET sensor, were significantly higher in week 12 compared
571 to week 6 hiPSC-CM (Fig. 7C). These results suggest the potential for higher activity
572 of mitochondrial calcium-dependent dehydrogenases (such as PDH or TCA cycle
573 enzymes) and a higher proton-motive force for oxidative ATP production.
574

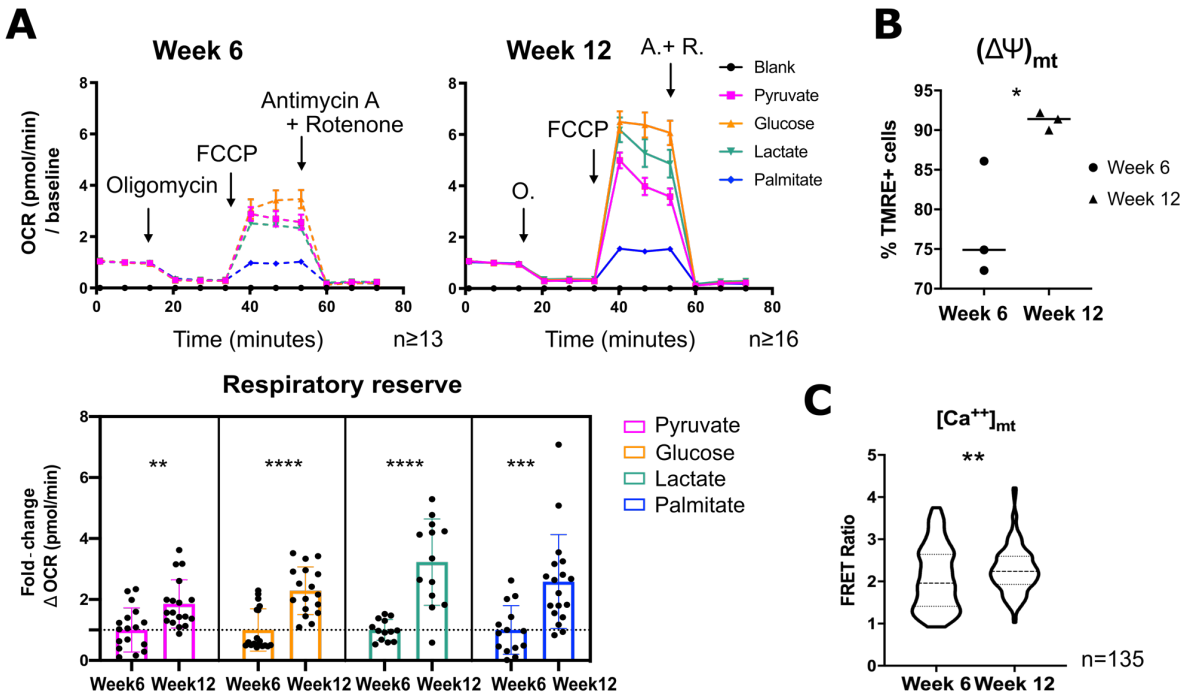

575

576 **Figure 7. Mitochondrial function in week 6 versus week 12 hiPSC-CM.** A)
577 Mitochondrial stress tests in week 6 versus week 12 hiPSC-CM provided with a single
578 substrate. Top panels show average OCR profiles, n⩾13 (week 6); n⩾16 (week 12)
579 profiles, from at least 3 independent differentiations, run on 4 separate plates. Bottom
580 panels show quantification of relative respiratory reserve. Data are mean ± S.E.M. **,
581 p<0.01; ***, p < 0.001; ****, p<0.0001 by Student t-test (if normal distributions were
582 confirmed by Shapiro-Wilk test) or non-parametric Mann-Whitney test. n⩾13 (week 6);

583 n⩾16 (week 12) wells of 4 Seahorse plates, from at least 3 independent
584 differentiations. B) Extrapolation of $(\Delta\Psi)_{mt}$ differences in TMRE-stained cells by flow
585 cytometry. Data are means. *, $p<0.05$ by unpaired t-test after normal distributions were
586 confirmed by Shapiro-Wilk test. n=3 independent differentiations (>10,000
587 cells/sample). C) Quantification of $[Ca^{++}]_{mt}$ by a mitochondrial-targeted Cameleon
588 FRET probe. Data are mean ± S.E.M. **, $p<0.01$ by non-parametric Mann-Whitney
589 test. n>135 individual cells from 3 independent differentiations.
590
591 To assess whether these improvements in the mitochondrial oxidative capacity
592 were due to altered mitochondrial content or mitochondrial network structure we
593 studied live cells labeled with Mitotracker® Green. 3D stacks were processed an
594 analyzed using the MiNa imageJ tool by the Stuart lab [30]. Cells from both stages
595 exhibited similar mitochondrial footprint (area of the cell occupied by mitochondria)
596 (Fig. 8A). This was confirmed in 2D fluorescent micrographs in which both cell size
597 and mitochondrial area per cell were similar between time-points (Suppl. Fig. 3A). An
598 unaltered mitochondrial content was corroborated by a similar nuclear/mitochondrial
599 DNA ratio between time-points (Fig. 8B). However, week 12 hiPSC-CM displayed
600 significantly higher mitochondrial network branching parameters such as the number
601 of branches per network and branch lengths (Fig. 8A and Suppl. Fig. 3C).
602 Ultrastructural examination of hiPSC-CM by transmission electron microscopy
603 confirmed enhanced branching in interfibrillar mitochondria in week 12 compared to
604 week 6 cells (Fig. 8C). 12 week hiPSC-CM showed longer mitochondria and a more
605 developed branching pattern. These changes are suggestive of a maturation of the
606 mitochondrial network.
607 The protein levels and phosphorylation of the transcription factor peroxisome
608 proliferator-activated receptor gamma coactivator 1-alpha (PGC1α), involved in
609 mitochondrial biogenesis [41], were no different in 12 week compared to 6 week
610 hiPSC-CM (Fig. 8D). Finally, the protein levels of different components of the ETC
611 were also similar between time points (Fig. 8E).

612 Collectively, these results indicate that the long-term culture of hiPSC-CM from
613 6 weeks to 12 weeks post-differentiation is accompanied by a structural and functional
614 maturation of the mitochondrial network, but no increase in mitochondrial content *per*
615 *se*.

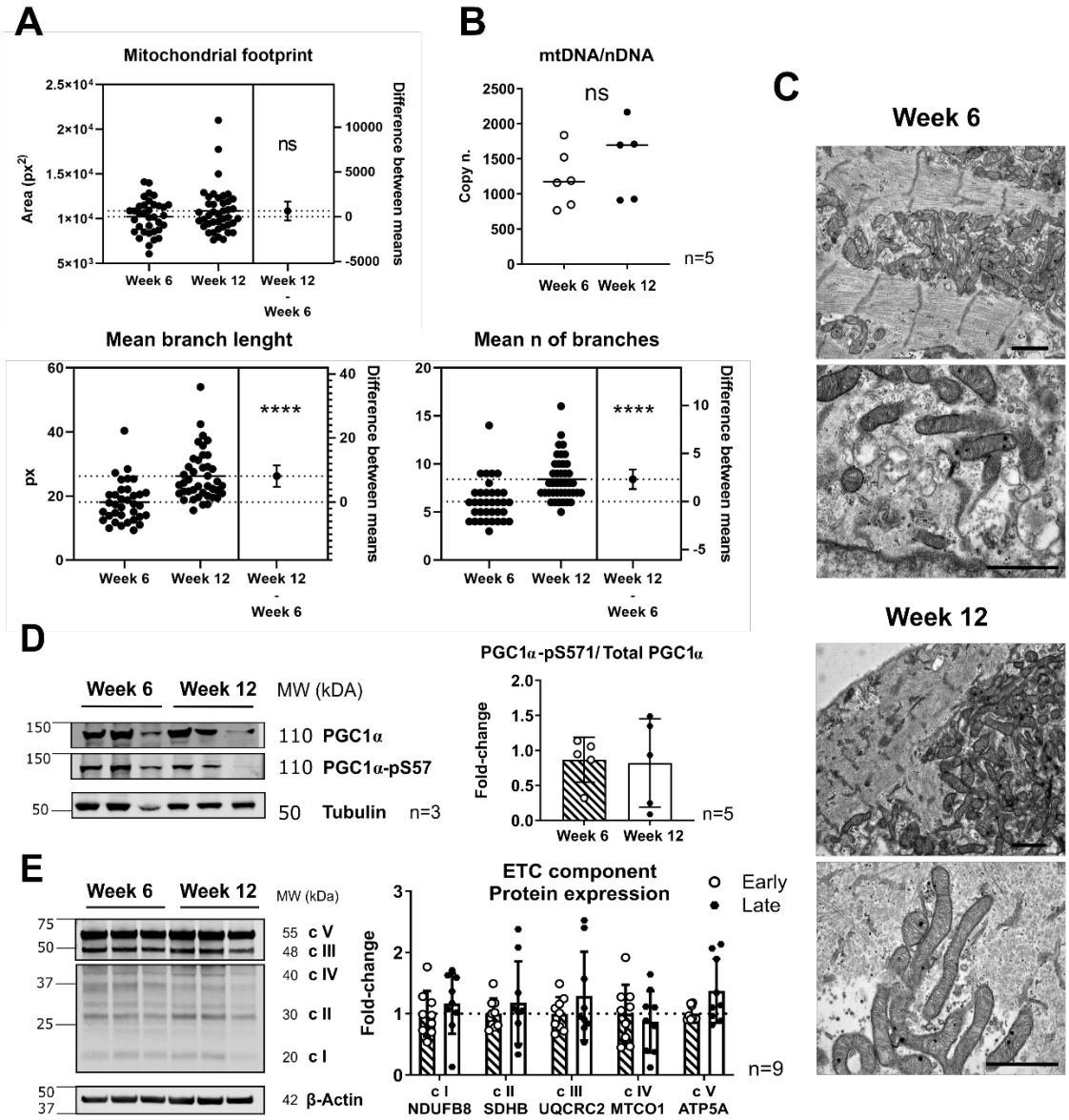

616

617 **Figure 8. Mitochondrial content and network structure in hiPSC-CM at week 6**
618 **versus week 12.** A) Mitochondrial network analysis (MiNa) [30], in Mitotracker®
619 Green stained cells via 3D stack live imaging. n>36 cells from 3 independent
620 differentiations. B) Mitochondrial DNA to nuclear DNA ratio. Data are mean ± S.D. not
621 significant by paired t-test; p=0.386; n=5 independent differentiation experiment. C)
622 Representative transmission electron micrographs of week 6 and week 12 hiPSC-CM
623 showing interfibrillar mitochondria. Scale bars: left, 1 µm; right, 2 µm. D-E) Left panels
624 show representative Western blots for the indicated proteins. Right panels show

quantification of blots. Data are mean ± S.D. n=3 (D); n=9 (E). ns by Student t-test or non-parametric Mann-Whitney test. PGC1α: PPARG (peroxisome proliferator activated receptor gamma) coactivator 1 alpha; ETC: electron transport chain; NDUFB8: NADH:ubiquinone oxidoreductase subunit B8; SDHB, succinate dehydrogenase subunit B; UQCRC2: ubiquinol cytochrome c reductase core protein 2; MTCO1: mitochondrial encoded cytochrome c oxidase I; ATP5A: ATP synthase subunit alpha.

632 **Discussion**

633

634 HiPSC-CM represent a powerful model system with remarkable potential for drug
635 discovery, disease modeling and regenerative medicine. A limitation of the model,
636 however, is the relatively immature phenotype of hiPSC-CM as compared to fully
637 differentiated CM in the heart. A variety of approaches are described to enhance the
638 maturation of hiPS-CM, including the maintenance in culture for prolonged periods
639 after their initial differentiation from hiPSC [5–7,42]. While the impact of such changes
640 on contractile function and electrophysiological characteristics has been studied
641 extensively, a detailed multi-modality analysis of the progressive maturation of
642 metabolic profile in these cells is lacking. This is especially important because energy
643 metabolism is fundamental in maintaining CM and heart function and is integrally
644 linked to physiological and pathophysiological CM growth and remodeling.
645 In this study, we have investigated the global metabolic profile of hiPSC-CM and the
646 changes during maturation in culture using a combination of methodologies such as
647 LC/MS metabolomics, ^{13}C-enrichment, extracellular flux analysis and readouts of
648 mitochondrial structure and function. We show that the metabolic profile of hiPSC-CM
649 cultured for 12 weeks changes considerably as compared to cells studied at the
650 standard time-point of 6 weeks after differentiation from hiPSC. The changes that we
651 identify resemble many of the changes that occur during the early post-natal
652 maturation of the mammalian heart.

653

654 **Anaerobic metabolism and glycolytic branch pathways**

655 Glycolytic flux as assessed either by U^{13}C-labeled glucose experiments or
656 quantification of ECAR using an extracellular flux analyzer revealed similar rates in
657 differentiated and long-term cultured hiPSC-CM, cultured in 10 mM glucose. This was

658 paralleled by an overall increase in oxidative phosphorylation such that the ratio
659 between OCR and ECAR was higher in long-term cultured myocytes when cells were
660 offered a variety of carbon substrates including BSA-conjugated palmitate.

661 Anaerobic metabolism is prevalent in stem cells and is associated with the
662 proliferative state [14]. The sustained rate of anaerobic glycolysis in hiPSC-CM at 12
663 weeks compared to 6 weeks may be related to the anabolic requirements of these
664 cells and could be involved in maintaining an immature phenotype. This hypothesis is
665 supported by recent data showing that inhibition of HIF1-α or LDHA, which promote
666 anaerobic metabolism, enhances the structural and functional maturation of hiPSC-
667 CM [43]. In the current study, it was of interest that although overall glycolysis rates
668 were similar between week 6 and week 12 hiPSC-CM, there were nevertheless
669 significant changes in some of the key enzymes in the pathway. A switch in the
670 expression from hexokinase 2 to hexokinase 1 occurred between 6 and 12 weeks
671 hiPSC-CM. Hexokinase 2 is usually expressed in highly proliferating cells (such as
672 stem cells and cancer cells), whereas hexokinase 1 associates with the mitochondrial
673 fraction and is important in the neonatal period for the coupling of glycolysis to
674 oxidative metabolism [44]. Moreover, the reduced abundance of proximal glycolytic
675 metabolites, measured via LC-MS, in long-term cultured hiPSC-CM, is consistent with
676 a shift to forward glycolysis rather than flux into branch pathways. Of note, while we
677 measured similar acidification rates between time-points, a proxy for lactate extrusion,
678 the expression of the lactate transporter MCT4 was markedly increased in long-term
679 cultured hiPSC-CM, suggesting that metabolic remodeling during maturation is
680 regulated by factors other than simply energy demands and utilization.

681 A small fraction of the glycolytic flux branches into the PPP. While metabolite
682 labelling analysis only suggested a marginal reduction in PPP flux with prolonged

683 culture, the expression levels of rate-limiting enzymes of the PPP were significantly
684 reduced. Given the essential role of the PPP in nucleotide synthesis [45], it is
685 reasonable to speculate that this could be linked to the time-dependent proliferative
686 decline of hiPSC-CMs. We also characterized aspects of the HBP and found a
687 significant reduction in GFAT2 expression and lower levels of UDP-GlcNAc in long-
688 term cultured cells, suggesting a reduction in HBP flux. At both stages OGT was highly
689 expressed, while OGA was scarcely detectable. Accordingly, there were no significant
690 changes in overall protein O-GlcNAcylation. It was recently shown in rats, that levels
691 of protein O-GlcNAcylation in the heart are maintained for the first 12 days of post-
692 natal life, and markedly declined by day 28 [46]. This was accompanied by a
693 concomitant reduction in GFAT (1 and 2) and OGT, while OGA was low at day 12 and
694 only became detectable at day 28, to further increase at later stages. Despite these
695 results deriving from rodents fed a high fat diet as a milk mimic, they can help
696 contextualize our hiPSC-CM cell model as resembling an early post-natal situation.
697

698 **Oxidative metabolism and substrate preference**

699 As glycolysis couples with oxidative metabolism, pyruvate enters the mitochondria,
700 where it is a substrate for the PDH complex. PDHα was found higher in 12 weeks
701 hiPSC-CM than less mature stages (Figure 3A). Stage-specific regulation of PDHα
702 phosphorylation by PDKs and PDPs, which determines the entry of glucose-derived
703 pyruvate into the TCA cycle, is well established in the perinatal heart [47,48]. We
704 observed a reduction in inhibitory phosphorylation of PDHα in long-term cultured
705 hiPSC-CM. PDK4 levels also increased 15-fold at this stage, while PDK1 was reduced,
706 similarly to what is observed in the early postnatal rat heart [47]. Such a change in

707 PDK expression is associated with an overall shift from glucose to fatty acids as
708 preferred oxidation fuel [49].

709 The utilization of different carbon substrates for oxidative phosphorylation and
710 energy production, and the changes in relative substrate usage after birth, are key
711 features of heart metabolism [13]. We developed a novel protocol to test the relative
712 contribution of different carbon sources to mitochondrial oxidative phosphorylation in
713 cells provided with a complete medium. A shift in substrate preference towards fatty
714 acids at the expense of glucose (when both substrates are present) distinguished
715 week 12 hiPSC-CM from cells at week 6. A similar remodeling is observed in early
716 postnatal heart development [13]. It is important to underline that these data do not
717 indicate an overall reduction in glucose oxidation. Indeed, in the absence of fatty acids,
718 we measured similar rates of anaerobic glycolysis and ATP-linked OCR. In complete
719 medium however, despite some variation between biological replicates, a marked shift
720 towards overall oxidative metabolism (OCR/ECAR) and an increase in relative BSA-
721 palmitate utilization characterized long-term cultured cells. It was also notable that
722 glutamine made a significant contribution to substrate utilization both at 6 and 12
723 weeks.

724 The increase in relative fatty acid oxidation in week 12 hiPSC-CM was
725 associated with increased expression of PPARα, the master regulator of fatty acid
726 metabolic enzymes. In line with this, the protein levels of several downstream targets
727 of PPARα signaling such as the fatty acid transporter CD36 and enzymes involved in
728 fatty acid oxidation were also increased at this stage. The fatty acid mitochondrial
729 shuttle CPT1 is sensitive to inhibition by Malonyl-CoA. The increased expression of
730 the mitochondrial-associated ACC isoform (ACC2), in week 12 hiPSC-CMs appears
731 puzzling. A possible interpretation resides in the increased capacity to transiently

732 regulate the mitochondrial import of fatty acids, accounting for higher metabolic
733 flexibility, typical of mature vs neonatal cardiac myocytes. In addition, the
734 electrophoretic shift of ACC1 (cytosolic isoform involved in fatty acid biosynthesis) may
735 be consistent with its inhibition by phosphorylation. However, this could not be directly
736 validated. MCD levels are known to increase during the early postnatal period [50].
737 This feature is not recapitulated in our prolonged culture model, where high levels of
738 MCD were detected by immunoblot at both time-points. These data do not exclude the
739 possibility that a progressive increase might have occurred at earlier time points.
740 Interestingly, we observed an overall increase in the capacity to oxidize any
741 individual substrate, evidenced by higher mitochondrial maximal respiration and spare
742 respiratory capacity for all substrates in week 12 hiPSC-CM. This may in part be
743 related to an increased expression and activity of key enzymes involved in the
744 utilization of glucose and fatty acids, but also suggests enhanced mitochondrial
745 capacity and higher metabolic flexibility in long-term cultured hiPSC-CMs.
746
747 **Mitochondrial function**
748 In the developing heart, an increase in CM mitochondrial content as well as a
749 structural and functional specialization, occur prenatally [41,51]. In our model, the
750 mitochondrial fraction assessed by MitoTracker Green® staining or mtDNA content
751 was not significantly different between the time-points studied. We also found no
752 differences in the protein levels of electron transport chain components nor in the
753 levels and post-translational phosphorylation of PCG1α, a key regulator of
754 mitogenesis and mitochondrial function [52]. This finding suggests that, any major
755 increase in mitochondrial content that occurred, might have done so earlier than week
756 6 after differentiation from hiPSCs. Indeed, it has been reported that a large increase

757 in mitochondrial content of hiPSC-CM occurs in the first 4 weeks after differentiation
758 [53]. However, further maturation of the mitochondria may continue significantly
759 beyond this period. Our mitochondrial network analysis and electron microscopy study
760 shows increased mitochondrial elongation and network branching in week 12 hiPSC-
761 CM as compared to early stages. In addition, the mitochondrial membrane potential
762 was significantly greater in late-stage hiPSC-CM along with a higher basal calcium
763 concentration in the matrix. These results indicate that a component of the increased
764 respiratory reserve and OCR in hiPSC-CM at week 12 may be ascribed to a maturation
765 of mitochondrial structure and function.

766 Taken together, these observations indicate an integrated maturation to an
767 early post-natal metabolic profile in week 12 hiPSC-CM.

768

769 Despite the significant changes in metabolic profile towards maturity that we
770 report in 2-dimensional (2D) cultures of hiPSC-CM, several important aspects need to
771 be considered when this preparation is used as a cardiac model. CM *in situ* are in a
772 3D environment and are subjected to a constant workload whereas the hiPSC-CM
773 model is largely unloaded. The metabolic profile under loaded conditions may
774 therefore be different. Furthermore, persistent loading of hiPSC-CM may itself alter
775 their maturation and metabolism [54–56]. Future studies in hiPSC-CM-derived
776 engineered heart muscle could address this question [57]. Paracrine and functional
777 interactions among different cell types in the multicellular heart may also alter the
778 metabolic profile [58]. Nevertheless, the 2D hiPSC-CM model is amenable to
779 pathophysiological and pharmacological manipulations to model in vivo conditions to
780 some extent, and can be easily scaled up, for example for screening purposes.

781 In conclusion, the data presented herein provide insights into the alterations in
782 metabolic profile of maturing hiPSC-CM in culture. The progressive restructuring of
783 cardiac-specific features in these cells indicates their potential to overcome the lack of
784 full maturation previously reported. The metabolic roadmap provided here may assist
785 in the design and interpretation of pathophysiological and pharmacological studies in
786 hiPSC-CM where metabolism plays an important role.
787

Acknowledgements

This work was supported by the British Heart Foundation (RE/18/2/34213 and CH/1999001/11735; AMS); a Fondation Leducq Transatlantic Network of Excellence award (17CVD04; AMS); the Department of Health via a National Institute for Health Research (NIHR) Biomedical Research Centre award to Guy's & St Thomas' NHS Foundation Trust in partnership with King's College London (IS-BRC-1215-20006; AMS); the Deutsche Forschungsgemeinschaft through the International Research Training Group Award (IRTG) 1816 (KSB, AMS); and the German Center for Cardiovascular Research (DZHK; KSB). GE was a Joint PhD student under IRTG 1816. We thank Roland Fleck and the Centre of Ultrastructural Imaging at King's College London for providing the equipment and expertise in electron microscopy.

We thank Katarzyna Kmiotek-Wasylewska, Sharwari Verma, Sandra Georgi, and Johanna Heine for the support provided.

Author contributions:

GE: conceptualization, experiments, data analysis, writing - original draft, review & editing; AZ: conceptualization, investigation, supervision, writing – review & editing; AP: contribution to experiments; CR: contribution to experiments; MC: contribution to experiments; MB: contribution to experiments; SR: contribution to experiments; KB: contribution to experiments; KSB: conceptualization, funding acquisition, supervision, editing final manuscript; AMS: conceptualization and experimental design, funding acquisition, supervision, writing – review & editing.

Disclosure of potential COI:

The authors declare no competing interests.

816 **References**

817

818 [1] D.T. Paik, M. Chandy, J.C. Wu, Patient and Disease-Specific Induced
819 Pluripotent Stem Cells for Discovery of Personalized Cardiovascular Drugs
820 and Therapeutics, Pharmacol. Rev. 72 (2020) 320–342.
821 https://doi.org/10.1124/pr.116.013003.

822 [2] C. Robertson, D.D. Tran, S.C. George, A. Manuscript, C. Cardiomyocytes, C.
823 Robertson, D.D. Tran, S.C. George, Concise review: Maturation phases of
824 human pluripotent stem cell-derived cardiomyocytes, Stem Cells. 31 (2013)
825 829–837. https://doi.org/10.1002/stem.1331.

826 [3] C.W. van den Berg, S. Okawa, S.M. Chuva de Sousa Lopes, L. van Iperen, R.
827 Passier, S.R. Braam, L.G. Tertoolen, A. Del Sol, R.P. Davis, C.L. Mummery,
828 Transcriptome of human foetal heart compared with cardiomyocytes from
829 pluripotent stem cells., Development. (2015) 3231–3238.
830 https://doi.org/10.1242/dev.123810.

831 [4] C.Y. Ivashchenko, G.C. Pipes, I.M. Lozinskaya, Z. Lin, X. Xiaoping, S. Needle,
832 E.T. Grygielko, E. Hu, J.R. Toomey, J.J. Lepore, R.N. Willette, Human-induced
833 pluripotent stem cell-derived cardiomyocytes exhibit temporal changes in
834 phenotype., Am. J. Physiol. Heart Circ. Physiol. 305 (2013) H913-22.
835 https://doi.org/10.1152/ajpheart.00819.2012.

836 [5] C. Correia, A. Koshkin, P. Duarte, D. Hu, A. Teixeira, I. Domian, M. Serra,
837 P.M. Alves, Distinct carbon sources affect structural and functional maturation
838 of cardiomyocytes derived from human pluripotent stem cells, Sci. Rep. 7
839 (2017) 1–17. https://doi.org/10.1038/s41598-017-08713-4.

840 [6] K. Ronaldson-Bouchard, S.P. Ma, K. Yeager, T. Chen, L.J. Song, D. Sirabella,
841 K. Morikawa, D. Teles, M. Yazawa, G. Vunjak-Novakovic, Advanced

842 maturation of human cardiac tissue grown from pluripotent stem cells, Nature.
843 556 (2018) 239–243. https://doi.org/10.1038/s41586-018-0016-3.
844 [7] D.A.M. Feyen, W.L. McKeithan, A.A.N. Bruyneel, S. Spiering, L. Hörmann, B.
845 Ulmer, H. Zhang, F. Briganti, M. Schweizer, B. Hegyi, Z. Liao, R.-P. Pölönen,
846 K.S. Ginsburg, C.K. Lam, R. Serrano, C. Wahlquist, A. Kreymerman, M. Vu,
847 P.L. Amatya, C.S. Behrens, S. Ranjbarvaziri, R.G.C. Maas, M. Greenhaw, D.
848 Bernstein, J.C. Wu, D.M. Bers, T. Eschenhagen, C.M. Metallo, M. Mercola,
849 Metabolic Maturation Media Improve Physiological Function of Human iPSC-
850 Derived Cardiomyocytes, Cell Rep. 32 (2020).
851 https://doi.org/10.1016/j.celrep.2020.107925.
852 [8] N. Hellen, C. Pinto Ricardo, K. Vauchez, G. Whiting, J.X. Wheeler, S.E.
853 Harding, Proteomic Analysis Reveals Temporal Changes in Protein
854 Expression in Human Induced Pluripotent Stem Cell-Derived Cardiomyocytes
855 In Vitro, Stem Cells Dev. 28 (2019) 565–578.
856 https://doi.org/10.1089/scd.2018.0210.
857 [9] G. Jung, G. Fajardo, A.J.S. Ribeiro, K.B. Kooiker, M. Coronado, M. Zhao, D.Q.
858 Hu, S. Reddy, K. Kodo, K. Sriram, P.A. Insel, J.C. Wu, B.L. Pruitt, D.
859 Bernstein, Time-dependent evolution of functional vs. remodeling signaling in
860 induced pluripotent stem cell-derived cardiomyocytes and induced maturation
861 with biomechanical stimulation, FASEB J. 30 (2016) 1464–1479.
862 https://doi.org/10.1096/fj.15-280982.
863 [10] T.G. Otsuji, I. Minami, Y. Kurose, K. Yamauchi, M. Tada, N. Nakatsuji,
864 Progressive maturation in contracting cardiomyocytes derived from human
865 embryonic stem cells: Qualitative effects on electrophysiological responses to
866 drugs, Stem Cell Res. 4 (2010) 201–213.

867 https://doi.org/https://doi.org/10.1016/j.scr.2010.01.002.
868 [11] W. Cai, J. Zhang, W.J. de Lange, Z.R. Gregorich, H. Karp, E.T. Farrell, S.D.
869 Mitchell, T. Tucholski, Z. Lin, M. Biermann, S.J. McIlwain, J.C. Ralphe, T.J.
870 Kamp, Y. Ge, An Unbiased Proteomics Method to Assess the Maturation of
871 Human Pluripotent Stem Cell–Derived Cardiomyocytes, Circ. Res. 125
872 (2019) 936–953. https://doi.org/10.1161/CIRCRESAHA.119.315305.
873 [12] A. Ebert, A.U. Joshi, S. Andorf, Y. Dai, S. Sampathkumar, H. Chen, Y. Li, P.
874 Garg, K. Toischer, G. Hasenfuss, D. Mochly-Rosen, J.C. Wu, Proteasome-
875 Dependent Regulation of Distinct Metabolic States During Long-Term Culture
876 of Human iPSC-Derived Cardiomyocytes, Circ. Res. 125 (2019) 90–103.
877 https://doi.org/10.1161/CIRCRESAHA.118.313973.
878 [13] G.D. Lopaschuk, J.S. Jaswal, Energy metabolic phenotype of the
879 cardiomyocyte during development, differentiation, and postnatal maturation,
880 J. Cardiovasc. Pharmacol. 56 (2010) 130–140.
881 https://doi.org/10.1097/FJC.0b013e3181e74a14.
882 [14] C. Hu, L. Fan, P. Cen, E. Chen, Z. Jiang, L. Li, Energy Metabolism Plays a
883 Critical Role in Stem Cell Maintenance and Differentiation, Int. J. Mol. Sci. 17
884 (2016) 253. https://doi.org/10.3390/ijms17020253.
885 [15] T. Ezashi, P. Das, R.M. Roberts, Low O2 tensions and the prevention of
886 differentiation of hES cells, Proc. Natl. Acad. Sci. U. S. A. 102 (2005) 4783–
887 4788. https://doi.org/10.1073/pnas.0501283102.
888 [16] B.N. Puente, W. Kimura, S.A. Muralidhar, J. Moon, J.F. Amatruda, K.L.
889 Phelps, D. Grinsfelder, B.A. Rothermel, R. Chen, J.A. Garcia, C.X. Santos, S.
890 Thet, E. Mori, M.T. Kinter, P.M. Rindler, S. Zacchigna, S. Mukherjee, D.J.
891 Chen, A.I. Mahmoud, M. Giacca, P.S. Rabinovitch, A. Aroumougame, A.M.

892 Shah, L.I. Szweda, H.A. Sadek, The oxygen-rich postnatal environment
893 induces cardiomyocyte cell-cycle arrest through DNA damage response, Cell.
894 157 (2014) 565–579. https://doi.org/10.1016/j.cell.2014.03.032.
895 [17] Y.M. Cho, S. Kwon, Y.K. Pak, H.W. Seol, Y.M. Choi, D.J. Park, K.S. Park, H.K.
896 Lee, Dynamic changes in mitochondrial biogenesis and antioxidant enzymes
897 during the spontaneous differentiation of human embryonic stem cells,
898 Biochem. Biophys. Res. Commun. 348 (2006) 1472–1478.
899 https://doi.org/https://doi.org/10.1016/j.bbrc.2006.08.020.
900 [18] L.I. Burd, M.D. Jones, M.A. Simmons, E.L. Makowski, G. Meschia, F.C.
901 Battaglia, Placental production and foetal utilisation of lactate and pyruvate,
902 Nature. 254 (1975) 710–711. https://doi.org/10.1038/254710a0.
903 [19] G.D. Lopaschuk, M.A. Spafford, D.R. Marsh, Glycolysis is predominant source
904 of myocardial ATP production immediately after birth, Am. J. Physiol. Circ.
905 Physiol. 261 (1991) H1698–H1705.
906 https://doi.org/10.1152/ajpheart.1991.261.6.H1698.
907 [20] P. Rana, B. Anson, S. Engle, Y. Will, Characterization of human-induced
908 pluripotent stem cell-derived cardiomyocytes: Bioenergetics and utilization in
909 safety screening, Toxicol. Sci. 130 (2012) 117–131.
910 https://doi.org/10.1093/toxsci/kfs233.
911 [21] T. Doenst, T.D. Nguyen, E.D. Abel, Cardiac Metabolism in Heart Failure
912 Implications Beyond ATP Production, Circ Res. 113,6 (2013) 709–724.
913 https://doi.org/10.1161/CIRCRESAHA.113.300376.
914 [22] K. Streckfuss-Bömeke, F. Wolf, A. Azizian, M. Stauske, K. Streckfuss-bo, R.
915 Dressel, S. Chen, M. Tiburcy, S. Wagner, D. Hu, L.S. Maier, G. Wulf, V.
916 Lorenz, M.P. Scho, W.H. Zimmermann, G. Hasenfuss, K. Guan, Comparative

917 study of human-induced pluripotent stem cells derived from bone marrow cells
918 , hair keratinocytes , and skin fibroblasts, Eur. Hear. J. 34 (2013) 2618–2629.
919 https://doi.org/10.1093/eurheartj/ehs203.
920 [23] T. Borchert, D. Hübscher, C.I. Guessoum, T.D.D. Lam, J.R. Ghadri, I.N.
921 Schellinger, M. Tiburcy, N.Y. Liaw, Y. Li, J. Haas, S. Sossalla, M.A. Huber, L.
922 Cyganek, C. Jacobshagen, R. Dressel, U. Raaz, V.O. Nikolaev, K. Guan, H.
923 Thiele, B. Meder, B. Wollnik, W.H. Zimmermann, T.F. Lüscher, G. Hasenfuss,
924 C. Templin, K. Streckfuss-Bömeke, Catecholamine-Dependent β-Adrenergic
925 Signaling in a Pluripotent Stem Cell Model of Takotsubo Cardiomyopathy, J.
926 Am. Coll. Cardiol. 70 (2017) 975–991.
927 https://doi.org/10.1016/j.jacc.2017.06.061.
928 [24] X. Lian, J. Zhang, S.M. Azarin, K. Zhu, L.B. Hazeltine, X. Bao, C. Hsiao, T.J.
929 Kamp, S.P. Palecek, Directed cardiomyocyte differentiation from human
930 pluripotent stem cells by modulating Wnt/β-catenin signaling under fully
931 defined conditions., Nat. Protoc. 8 (2013) 162–75.
932 https://doi.org/10.1038/nprot.2012.150.
933 [25] S. Tohyama, F. Hattori, M. Sano, T. Hishiki, Y. Nagahata, T. Matsuura, H.
934 Hashimoto, T. Suzuki, H. Yamashita, Y. Satoh, T. Egashira, T. Seki, N.
935 Muraoka, H. Yamakawa, Y. Ohgino, T. Tanaka, M. Yoichi, S. Yuasa, M.
936 Murata, M. Suematsu, K. Fukuda, Distinct metabolic flow enables large-scale
937 purification of mouse and human pluripotent stem cell-derived cardiomyocytes,
938 Cell Stem Cell. 12 (2013) 127–137. https://doi.org/10.1016/j.stem.2012.09.013.
939 [26] M. Schnelle, M. Chong, A. Zoccarato, M. Elkenani, G.J. Sawyer, G.
940 Hasenfuss, C. Ludwig, A.M. Shah, In vivo [U-13C]-glucose labeling to assess
941 heart metabolism in murine models of pressure and volume overload, Am. J.

942 Physiol. Circ. Physiol. (2020). https://doi.org/10.1152/ajpheart.00219.2020.
943 [27] C. Ludwig, U.L. Günther, MetaboLab - advanced NMR data processing and
944 analysis for metabolomics, BMC Bioinformatics. 12 (2011) 366.
945 https://doi.org/10.1186/1471-2105-12-366.
946 [28] S.C. Sapcariu, T. Kanashova, D. Weindl, J. Ghelfi, G. Dittmar, K. Hiller,
947 Simultaneous extraction of proteins and metabolites from cells in culture,
948 MethodsX. 1 (2014) 74–80.
949 https://doi.org/https://doi.org/10.1016/j.mex.2014.07.002.
950 [29] Z. Pang, J. Chong, G. Zhou, D.A. de Lima Morais, L. Chang, M. Barrette, C.
951 Gauthier, P.-É. Jacques, S. Li, J. Xia, MetaboAnalyst 5.0: narrowing the gap
952 between raw spectra and functional insights, Nucleic Acids Res. 49 (2021)
953 W388–W396. https://doi.org/10.1093/nar/gkab382.
954 [30] A.J. Valente, L.A. Maddalena, E.L. Robb, F. Moradi, J.A. Stuart, A simple
955 ImageJ macro tool for analyzing mitochondrial network morphology in
956 mammalian cell culture, Acta Histochem. 119 (2017) 315–326.
957 https://doi.org/10.1016/j.acthis.2017.03.001.
958 [31] M. Beretta, C.X.C. Santos, C. Molenaar, A.D. Hafstad, C.C.J. Miller, A.
959 Revazian, K. Betteridge, K. Schröder, K. Streckfuß-Bömeke, J.H. Doroshow,
960 R.A. Fleck, T.-P. Su, V. V Belousov, M. Parsons, A.M. Shah, Nox4 regulates
961 InsP3 receptor-dependent Ca2+ release into mitochondria to promote cell
962 survival, EMBO J. n/a (2020) e103530.
963 https://doi.org/10.15252/embj.2019103530.
964 [32] X. Lian, C. Hsiao, G. Wilson, K. Zhu, L.B. Hazeltine, S.M. Azarin, K.K. Raval,
965 J. Zhang, T.J. Kamp, S.P. Palecek, Robust cardiomyocyte differentiation from
966 human pluripotent stem cells via temporal modulation of canonical Wnt

967 signaling, Proc. Natl. Acad. Sci. 109 (2012) E1848–E1857.
968 https://doi.org/10.1073/pnas.1200250109.
969 [33] F.B. Bedada, M. Wheelwright, J.M. Metzger, Maturation status of sarcomere
970 structure and function in human iPSC-derived cardiac myocytes, Biochim.
971 Biophys. Acta - Mol. Cell Res. 1863 (2016) 1829–1838.
972 https://doi.org/10.1016/j.bbamcr.2015.11.005.
973 [34] T. Kamakura, T. Makiyama, K. Sasaki, Y. Yoshida, Y. Wuriyanghai, J. Chen,
974 T. Hattori, S. Ohno, T. Kita, M. Horie, S. Yamanaka, T. Kimura, Ultrastructural
975 Maturation of Human-Induced Pluripotent Stem Cell-Derived Cardiomyocytes
976 in a Long-Term Culture, Circ. J. 77 (2013) 1307–1314.
977 https://doi.org/10.1253/circj.CJ-12-0987.
978 [35] S. Chung, D.K. Arrell, R.S. Faustino, A. Terzic, P.P. Dzeja, Glycolytic network
979 restructuring integral to the energetics of embryonic stem cell cardiac
980 differentiation, J. Mol. Cell. Cardiol. 48 (2010) 725–734.
981 https://doi.org/10.1016/j.yjmcc.2009.12.014.
982 [36] M.J. Rardin, S.E. Wiley, R.K. Naviaux, A.N. Murphy, J.E. Dixon, Monitoring
983 phosphorylation of the pyruvate dehydrogenase complex, Anal. Biochem. 389
984 (2009) 157–164. https://doi.org/10.1016/j.ab.2009.03.040.
985 [37] G.W. Goodwin, D.M. Cohen, H. Taegtmeyer, [5-3H]glucose overestimates
986 glycolytic flux in isolated working rat heart: role of the pentose phosphate
987 pathway, Am. J. Physiol. Metab. 280 (2001) E502–E508.
988 https://doi.org/10.1152/ajpendo.2001.280.3.E502.
989 [38] G.A. Ngoh, H.T. Facundo, A. Zafir, S.P. Jones, O-GlcNAc signaling in the
990 cardiovascular system, Circ. Res. 107 (2010) 171–185.
991 https://doi.org/10.1161/CIRCRESAHA.110.224675.

[39] G.A. J., van der L.K. A.J.M., W.P. H.M., C. Giulia, van der L.F. R., van der V.G. J., S. Bart, van B. Marc, Peroxisome Proliferator-Activated Receptor (PPAR) α and PPARβ/δ, but not PPARγ, Modulate the Expression of Genes Involved in Cardiac Lipid Metabolism, Circ. Res. 92 (2003) 518–524. https://doi.org/10.1161/01.RES.0000060700.55247.7C.

[40] D.W. Foster, Malonyl-CoA: the regulator of fatty acid synthesis and oxidation, J. Clin. Invest. 122 (2012) 1958–1959. https://doi.org/10.1172/JCI63967.

[41] J.J. Lehman, P.M. Barger, A. Kovacs, J.E. Saffitz, D.M. Medeiros, D.P. Kelly, Peroxisome proliferator–activated receptor γ coactivator-1 promotes cardiac mitochondrial biogenesis, J. Clin. Invest. 106 (2000) 847–856. https://doi.org/10.1172/JCI10268.

[42] C.A. Lopez, H.H.A.A. Al-Siddiqi, U. Purnama, S. Iftekhar, A.A.N. Bruyneel, M. Kerr, R. Nazir, M. da Luz Sousa Fialho, S. Malandraki-Miller, R. Alonaizan, F. Kermani, L.C. Heather, J. Czernuszka, C.A. Carr, Physiological and pharmacological stimulation for in vitro maturation of substrate metabolism in human induced pluripotent stem cell-derived cardiomyocytes, Sci. Rep. 11 (2021) 7802. https://doi.org/10.1038/s41598-021-87186-y.

[43] D. Hu, A. Linders, A. Yamak, C. Correia, J.D. Kijlstra, A. Garakani, L. Xiao, D.J. Milan, P. van der Meer, M. Serra, P.M. Alves, I.J. Domian, Metabolic Maturation of Human Pluripotent Stem Cell-Derived Cardiomyocytes by Inhibition of HIF1alpha; and LDHA, Circ. Res. 123 (2018) 1066–1079. https://doi.org/10.1161/CIRCRESAHA.118.313249.

[44] H.L. Fritz, I.W. Smoak, S. Branch, Hexokinase I expression and activity in embryonic mouse heart during early and late organogenesis, Histochem. Cell Biol. 112 (1999) 359–365. https://doi.org/10.1007/s004180050417.

1017 [45] H.-G. Zimmer, The oxidative pentose phosphate pathway in the heart:
1018 Regulation, physiologicla significance, and clinical implications, Basic Res.
1019 Cardiol. 87 (1992) 303–316. https://doi.org/10.1007/BF00796517.
1020 [46] T. Dupas, M. Denis, J. Dontaine, A. Persello, L. Bultot, A. Erraud, D.
1021 Vertommen, B. Bouchard, A. Tessier, M. Rivière, J. Lebreton, E. Bigot-Corbel,
1022 J. Montnach, M. De Waard, C. Gauthier, Y. Burelle, A.K. Olson, B. Rozec, C.
1023 Des Rosiers, L. Bertrand, T. Issad, B. Lauzier, Protein O-GlcNAcylation levels
1024 are regulated independently of dietary intake in a tissue and time-specific
1025 manner during rat postnatal development, Acta Physiol. 231 (2021) 1–15.
1026 https://doi.org/10.1111/apha.13566.
1027 [47] M.C. Sugden, M.L. Langdown, R.A. Harris, M.J. Holness, Expression and
1028 regulation of pyruvate dehydrogenase kinase isoforms in the developing rat
1029 heart and in adulthood: role of thyroid hormone status and lipid supply,
1030 Biochem. J. 352 (2000) 731. https://doi.org/10.1042/0264-6021:3520731.
1031 [48] M.C. Sugden, M.J. Holness, Recent advances in mechanisms regulating
1032 glucose oxidation at the level of the pyruvate dehydrogenase complex by
1033 PDKs, Am. J. Physiol. - Endocrinol. Metab. 284 (2003) E855–E862.
1034 https://doi.org/10.1152/ajpendo.00526.2002.
1035 [49] I.K.N. Pettersen, D. Tusubira, H. Ashrafi, S.E. Dyrstad, L. Hansen, X.-Z. Liu,
1036 L.I.H. Nilsson, N.G. Løvsletten, K. Berge, H. Wergedahl, B. Bjørndal, Ø. Fluge,
1037 O. Bruland, A.C. Rustan, N. Halberg, G.V. Røsland, R.K. Berge, K.J. Tronstad,
1038 Upregulated PDK4 expression is a sensitive marker of increased fatty acid
1039 oxidation, Mitochondrion. 49 (2019) 97–110.
1040 https://doi.org/https://doi.org/10.1016/j.mito.2019.07.009.
1041 [50] M.A. Yatscoff, J.S. Jaswal, M.R. Grant, R. Greenwood, T. Lukat, D.L. Beker,

1042 I.M. Rebeyka, G.D. Lopaschuk, Myocardial Hypertrophy and the Maturation of
1043 Fatty Acid Oxidation in the Newborn Human Heart, Pediatr. Res. 64 (2008)
1044 643.
1045 [51] J.L. Pohjoismäki, S. Goffart, The role of mitochondria in cardiac development
1046 and protection, Free Radic. Biol. Med. 106 (2017) 345–354.
1047 https://doi.org/10.1016/j.freeradbiomed.2017.02.032.
1048 [52] M.J. Birket, S. Casini, G. Kosmidis, D.A. Elliott, A.A. Gerencser, A.
1049 Baartscheer, C. Schumacher, P.G. Mastroberardino, A.G. Elefanty, E.G.
1050 Stanley, C.L. Mummery, PGC-1α and Reactive Oxygen Species Regulate
1051 Human Embryonic Stem Cell-Derived Cardiomyocyte Function, Stem Cell
1052 Reports. 1 (2013) 560–574.
1053 https://doi.org/https://doi.org/10.1016/j.stemcr.2013.11.008.
1054 [53] D.-F. Dai, M.E. Danoviz, B. Wiczer, M.A. Laflamme, R. Tian, Mitochondrial
1055 Maturation in Human Pluripotent Stem Cell Derived Cardiomyocytes, Stem
1056 Cells Int. 2017 (2017) 1–10. https://doi.org/10.1155/2017/5153625.
1057 [54] T.J. Kolanowski, C.L. Antos, K. Guan, Making human cardiomyocytes up to
1058 date: Derivation, maturation state and perspectives, Int. J. Cardiol. 241 (2017)
1059 379–386. https://doi.org/10.1016/j.ijcard.2017.03.099.
1060 [55] P. Machiraju, S.C. Greenway, Current methods for the maturation of induced
1061 pluripotent stem cell-derived cardiomyocytes, World J. Stem Cells. 11 (2019)
1062 33–43. https://doi.org/10.4252/wjsc.v11.i1.33.
1063 [56] B.M. Ulmer, A. Stoehr, M.L. Schulze, S. Patel, M. Gucek, I. Mannhardt, S.
1064 Funcke, E. Murphy, T. Eschenhagen, A. Hansen, Contractile Work Contributes
1065 to Maturation of Energy Metabolism in hiPSC-Derived Cardiomyocytes, Stem
1066 Cell Reports. 10 (2018) 834–847.

1067 https://doi.org/https://doi.org/10.1016/j.stemcr.2018.01.039.
1068 [57] T. Malte, H.J. E., B. Paul, S. Susanne, M. Tim, C.L. Mei-Ling, L. Elif, R. Farah,
1069 Z. Sebastian, W. Edgar, R. Johannes, W. Mouer, G.J. D., K. Izhak, W. Erich,
1070 R. Ursula, D. Pieterjan, van L.L. W., G.M. Jose, K. Sara, T. Karl, H. Gerd, C.L.
1071 A., U. Andreas, L.W. A., A. Toshiyuki, N. Benjamin, K. Gordon, G. Lior, W.J.
1072 C., Z. Wolfram-Hubertus, Defined Engineered Human Myocardium With
1073 Advanced Maturation for Applications in Heart Failure Modeling and Repair,
1074 Circulation. 135 (2017) 1832–1847.
1075 https://doi.org/10.1161/CIRCULATIONAHA.116.024145.
1076 [58] E. Giacomelli, V. Meraviglia, G. Campostrini, A. Cochrane, X. Cao, R.W.J. van
1077 Helden, A. Krotenberg Garcia, M. Mircea, S. Kostidis, R.P. Davis, B.J. van
1078 Meer, C.R. Jost, A.J. Koster, H. Mei, D.G. Míguez, A.A. Mulder, M. Ledesma-
1079 Terrón, G. Pompilio, L. Sala, D.C.F. Salvatori, R.C. Slieker, E. Sommariva,
1080 A.A.F. de Vries, M. Giera, S. Semrau, L.G.J. Tertoolen, V. V Orlova, M. Bellin,
1081 C.L. Mummery, Human-iPSC-Derived Cardiac Stromal Cells Enhance
1082 Maturation in 3D Cardiac Microtissues and Reveal Non-cardiomyocyte
1083 Contributions to Heart Disease, Cell Stem Cell. 26 (2020) 862-879.e11.
1084 https://doi.org/10.1016/j.stem.2020.05.004.
1085
1086

1087 **Suppl. Figure 1.**

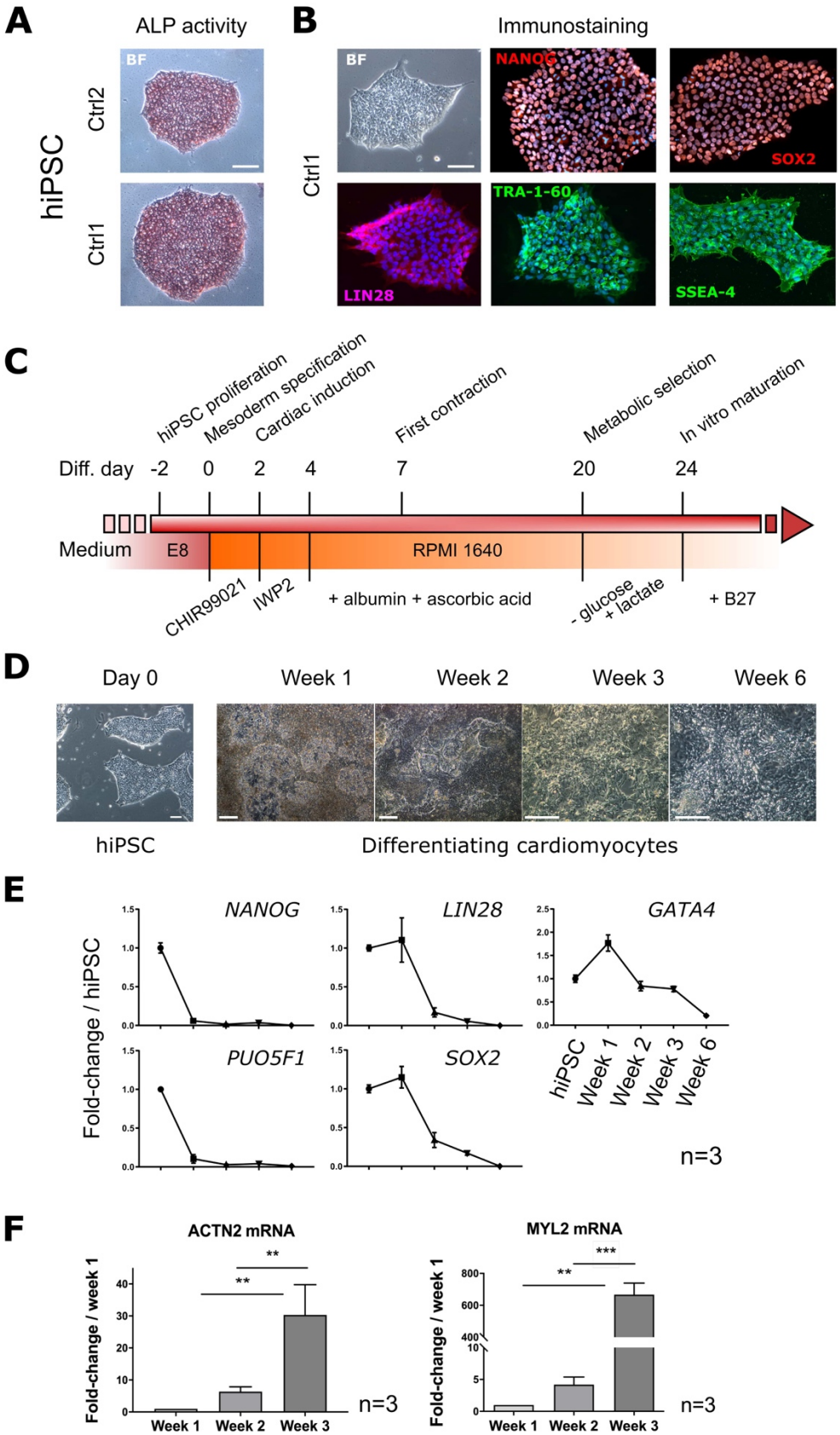

1088
1089

1090 **Supplementary Figure 1. Characterization of hiPSC differentiation to**
1091 **cardiomyocytes.** A) Representative images of alkaline phosphatase (ALP) activity in
1092 the two hiPSC lines utilized in this study (Ctrl1 and Ctrl2). Red staining, positive for
1093 ALP activity. Scale bar, 100 µm. B) Representative images of immunofluorescence for
1094 markers of pluripotency (NANOG, SOX2, LIN28, TRA-1-60, SSEA4). Scale bar, 200
1095 µm. BF: bright field. C) Schematic of the hiPSC-CM differentiation protocol.
1096 CHIR99021: inhibitor of glycogen-synthase kinase subunit 3; IWP2: inhibitor of Wnt
1097 signaling; Albumin: human recombinant; B27: growth supplement. D) Brightfield
1098 images of the time-course of hiPSC-CM differentiation. Scale bar, 200 µm. E) Time-
1099 course of changes in mRNA levels of pluripotency (*NANOG, LIN28, POU5F1, SOX2*)
1100 and cardiac-specification marker (*GATA4*) in differentiating hiPSC-CM. Data are mean
1101 ± S.D. Significances by 1-way ANOVA and Tukey's test for multiple comparisons are
1102 shown in Suppl. Table 5; n=3 independent differentiation experiments. F) Time-course
1103 of changes in mRNA levels of cardiac sarcomeric proteins in differentiating hiPSC-
1104 CM. Data are mean + S.D. **, $p<0.01$, ***, $p<0.001$ by Kruskal-Wallis 1-way analysis
1105 of variance and Dunn's correction; n=3 independent differentiation experiments.
1106

1107 **Suppl. Figure 2**

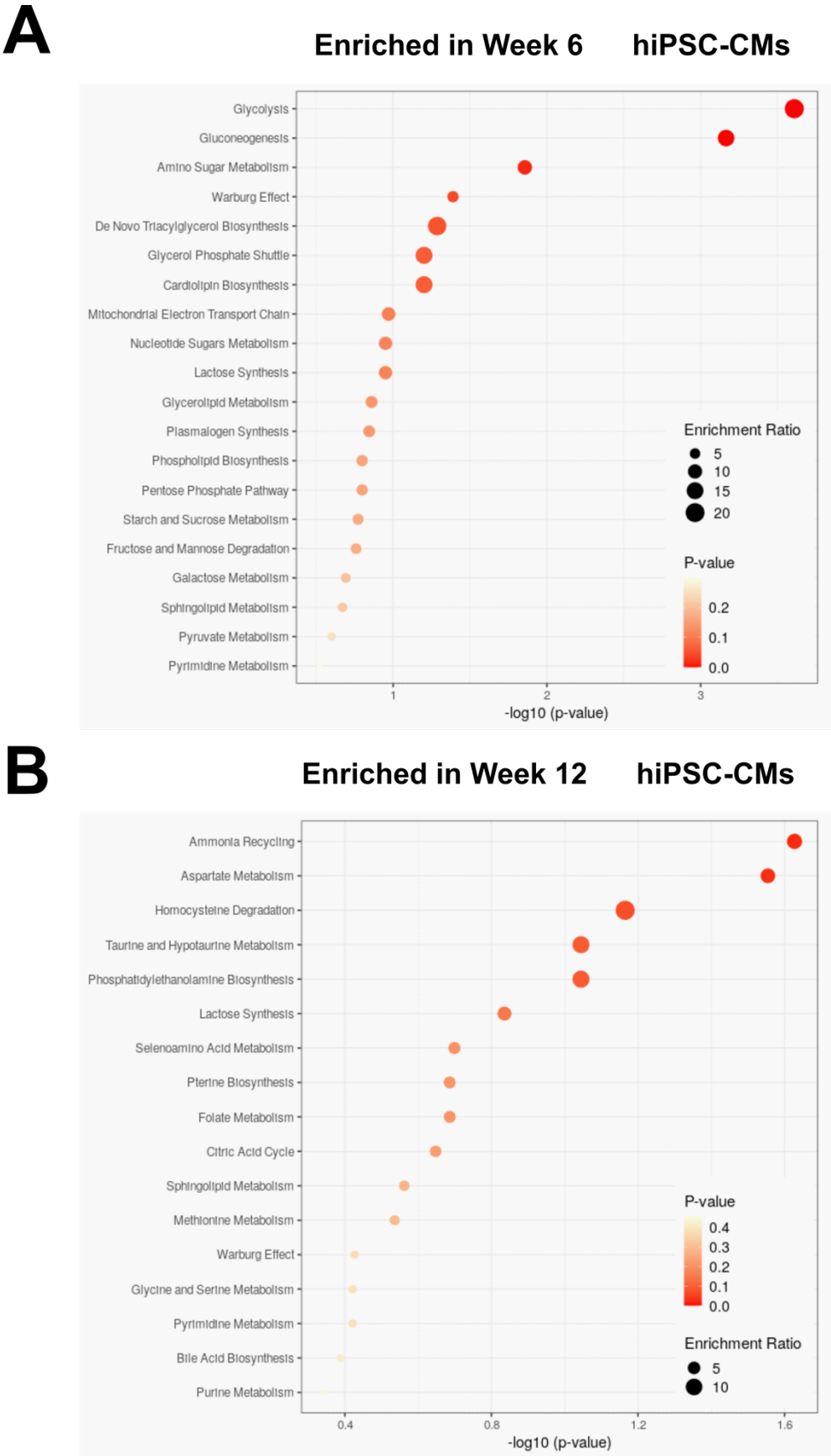

1108

1109 **Supplementary Figure 2.** Enrichment Analysis of significantly changed metabolites
1110 between week 6 and week 12 hiPSC-CMs. An Over Representation Analysis (ORA)
1111 was performed with metabolites that were significantly higher abundant in A) week 6
1112 and B) week 12 hiPSC-CMs. ORA was implemented using the hypergeometric test to
1113 evaluate whether a particular metabolite set is represented more than expected by
1114 chance. One-tailed p-values are provided after adjusting for multiple testing.
1115
1116

1117 **Suppl. Figure 3**
1118

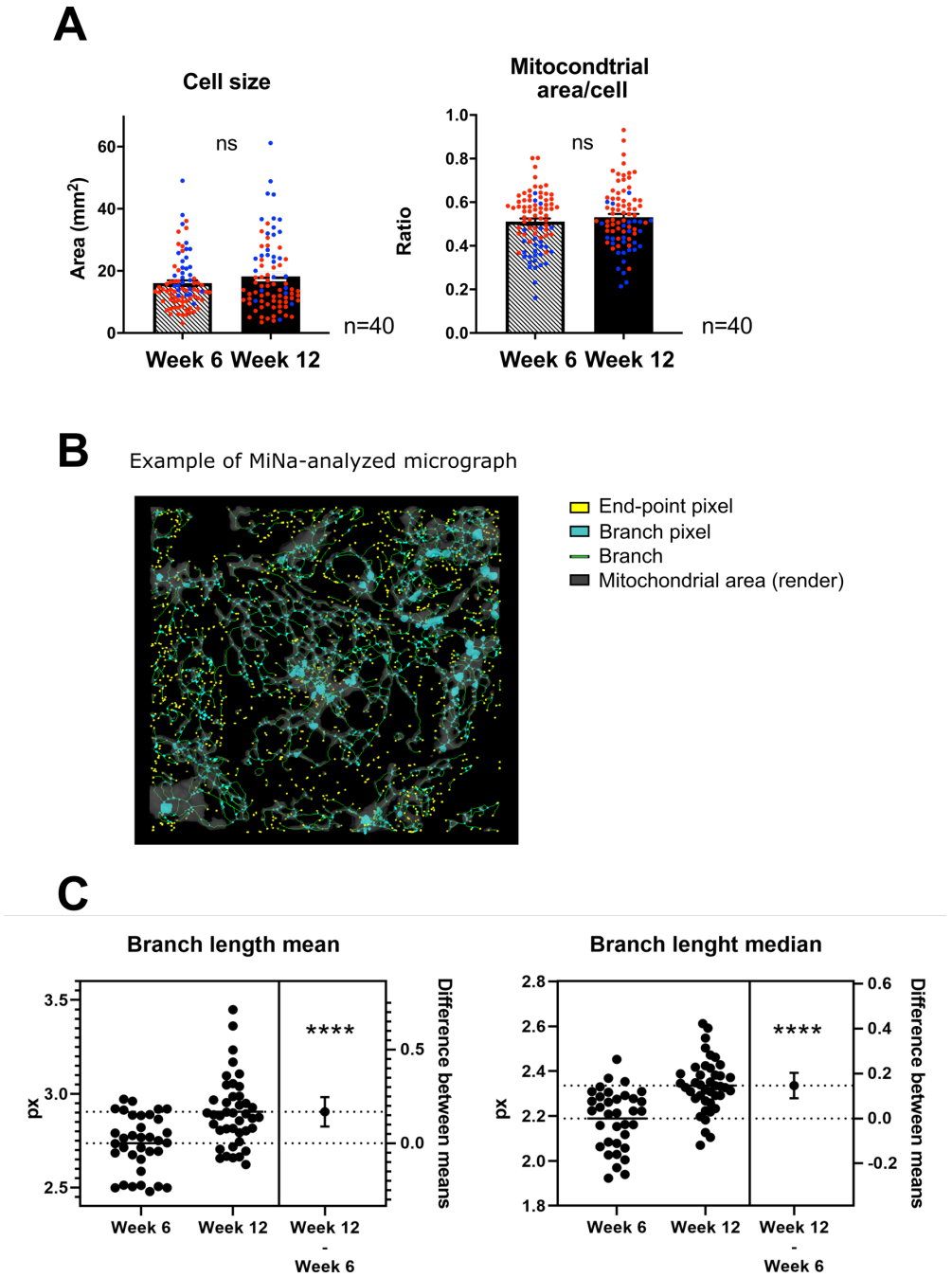

1119
1120
1121 **Supplementary Figure 3. Analysis of mitochondrial content and network**
1122 **structure.** A) Left: quantification of cell size by bright field microscopy. Right:
1123 quantification of mitochondrial area/cell area in cells loaded with Mitotracker® Green.
1124 Different colors represent different cardiac differentiations. n=40 iPSC-CM of 3
1125 differentiations. Ns, A: p=0.162; B: p=0.336; not significant by unpaired t-test. B)
1126 Example of z-stack analysis with MiNa [30] in week 6 hiPSC-CMs. C) Mitochondrial
1127 network analysis (MiNa), in Mitotracker® Green stained cells via 3D stack live imaging.
1128 n≥36 iPSC-CM of 3 independent differentiations.

1129 **Supplementary Table 5. 1-way ANOVA of data in Suppl. Fig. 1E**

	Alpha	**0,05**			
	Tukey's multiple comparisons test	Mean Diff,	95,00% CI of diff,	Summary	Adjusted P Value
NANOG	hiPSCs vs. Week 1	0,94	0,8035 to 1,077	****	<0,0001
	hiPSCs vs. Week 2	0,9841	0,8475 to 1,121	****	<0,0001
	hiPSCs vs. Week 3	0,964	0,8113 to 1,117	****	<0,0001
	hiPSCs vs. Week 6	0,9987	0,871 to 1,126	****	<0,0001
	Week 1 vs. Week 2	0,04407	-0,09252 to 0,1807	ns	0,8213
	Week 1 vs. Week 3	0,02394	-0,1288 to 0,1767	ns	0,9837
	Week 1 vs. Week 6	0,05868	-0,06909 to 0,1864	ns	0,5781
	Week 2 vs. Week 3	-0,02013	-0,1728 to 0,1326	ns	0,9915
	Week 2 vs. Week 6	0,01461	-0,1132 to 0,1424	ns	0,995
	Week 3 vs. Week 6	0,03474	-0,1101 to 0,1796	ns	0,9281
POU5F1	hiPSCs vs. Week 1	0,8968	0,7101 to 1,083	****	<0,0001
	hiPSCs vs. Week 2	0,972	0,7768 to 1,167	****	<0,0001
	hiPSCs vs. Week 3	0,96	0,6649 to 1,255	****	<0,0001
	hiPSCs vs. Week 6	0,9891	0,7558 to 1,222	****	<0,0001
	Week 1 vs. Week 2	0,07523	-0,09621 to 0,2467	ns	0,6161
	Week 1 vs. Week 3	0,06319	-0,2168 to 0,3431	ns	0,9411
	Week 1 vs. Week 6	0,09235	-0,1215 to 0,3062	ns	0,629
	Week 2 vs. Week 3	-0,01204	-0,2978 to 0,2737	ns	>0,9999
	Week 2 vs. Week 6	0,01712	-0,2042 to 0,2384	ns	0,9989
	Week 3 vs. Week 6	0,02916	-0,2838 to 0,3422	ns	0,9977
LIN28	hiPSCs vs. Week 1	-0,1043	-0,6784 to 0,4699	ns	0,9742
	hiPSCs vs. Week 2	0,8289	0,2547 to 1,403	**	0,0049
	hiPSCs vs. Week 3	0,9443	0,3702 to 1,518	**	0,0018
	hiPSCs vs. Week 6	0,9998	0,4627 to 1,537	***	0,0007
	Week 1 vs. Week 2	0,9332	0,359 to 1,507	**	0,002
	Week 1 vs. Week 3	1,049	0,4745 to 1,623	***	0,0008
	Week 1 vs. Week 6	1,104	0,567 to 1,641	***	0,0003
	Week 2 vs. Week 3	0,1154	-0,4587 to 0,6896	ns	0,963
	Week 2 vs. Week 6	0,1709	-0,3662 to 0,708	ns	0,837
	Week 3 vs. Week 6	0,05547	-0,4816 to 0,5925	ns	0,9969
SOX2	hiPSCs vs. Week 1	-0,1494	-0,5176 to 0,2188	ns	0,6776
	hiPSCs vs. Week 2	0,6612	0,293 to 1,029	**	0,0011
	hiPSCs vs. Week 3	0,8293	0,4176 to 1,241	***	0,0004
	hiPSCs vs. Week 6	0,9979	0,6534 to 1,342	****	<0,0001

	Week 1 vs. Week 2	0,8106	0,4424 to 1,179	***	0,0002
	Week 1 vs. Week 3	0,9787	0,567 to 1,39	***	0,0001
	Week 1 vs. Week 6	1,147	0,8028 to 1,492	****	<0,0001
	Week 2 vs. Week 3	0,1681	-0,2436 to 0,5798	ns	0,6728
	Week 2 vs. Week 6	0,3367	-0,007725 to 0,6811	ns	0,0561
	Week 3 vs. Week 6	0,1686	-0,2219 to 0,5592	ns	0,6293
GATA4	hiPSCs vs. Week 1	-0,7682	-1,229 to -0,3071	**	0,0019
	hiPSCs vs. Week 2	0,1574	-0,3037 to 0,6186	ns	0,7912
	hiPSCs vs. Week 3	0,2206	-0,295 to 0,7361	ns	0,6365
	hiPSCs vs. Week 6	0,7949	0,3636 to 1,226	***	0,0009
	Week 1 vs. Week 2	0,9257	0,4646 to 1,387	***	0,0004
	Week 1 vs. Week 3	0,9888	0,4733 to 1,504	***	0,0006
	Week 1 vs. Week 6	1,563	1,132 to 1,994	****	<0,0001
	Week 2 vs. Week 3	0,06314	-0,4524 to 0,5787	ns	0,9935
	Week 2 vs. Week 6	0,6374	0,2061 to 1,069	**	0,0046
	Week 3 vs. Week 6	0,5743	0,08521 to 1,063	*	0,0206

1131 **Supplementary experimental procedures**

1132

1133 **Supplementary Table 1. Primer sequences for RT-qPCR**

1134

TARGET GENE	FORWARD 5' -> 3'	REVERSE 5' -> 3'
ACTN2	TGCCTGATCTCCATGGGTTAC	GGCCTGGAATGTCACTACCC
B2M	TGCTGTCTCCATGTTTGATGTATCT	TCTCTGCTCCCCACCTCTAAGT
LIN28	CCCCCAGTGGATGTCTTTGT	CTCACCCTCCTTCAAGCTCC
MYL2	GGGCGGAGTGTGGAATTCTT	CCCGGCTCTCTTCTTTGCTT
NANOG	TGCAAGAACTCTCCAACATCC	GCTATTCTTCGGCCAGTTGTT
PUO5F1	GGGGTTCTATTTGGGAAGGTAT	GCCGCAGCTTACACATGTTC
SOX2	GGCAATAGCATGGCGAGC	TTCATGTGCGCGTAACTGTC

1135

1136 ACTN: actinin; B2M: beta 2 microglobulin; LIN28: abnormal cell LINeage; MYL:
1137 myosin light chain; NANOG: nanog homeobox; POU5F1: POU domain, class 5,
1138 transcription factor 1; SOX: Sry-type homebox.

1139

1140

1141 **Supplementary Table 2. Antibodies for immunostaining and FACS**

1142

TARGET PROTEIN	SPECIES	DILUTION	CATALOGUE #
ACTININ	Rabbit	1:500 (1:750 FACS)	Abcam, ab68194
cTNT	Mouse	1:750	Thermo Fisher, MS-295-PAbx
LIN28	Goat	1:300	R&D, AF3757
MLC2V	Rabbit	1:333 (1:250 FACS)	Proteintech, 10906-1-AP
NANOG	Rabbit	1:100	Thermo Fisher, PA1-097
OCT4	Goat	1:500	R&D, AF1759
SSEA-4	Mouse	1:200	Abcam, ab16287
SOX2	Mouse	1:200	R&D, MAB2018
TITIN C-TERM	Rabbit	1:750	Myomedix, TTN-M
TITIN N-TERM	Rabbit	1:750	Myomedix, TTN-Z
TRA-1-60	Mouse	1:200	Abcam, ab16288

1143

1144 cTNT: cardiac troponin T; LIN: abnormal cell LINeage; MLC: myosin light chain; OCT:
1145 octamer binding transcription factor; SSEA: stage specific embryo antigen; SOX: Sry-
1146 type homeobox; TRA: T cell receptor alpha locus.

1147

1148 **Supplementary Table 3. Antibodies for western blotting**

TARGET PROTEIN	SPECIES	DILUTION	CATALOGUE #
α-TUBULIN	Rat	1:2000	Santa Cruz, sc-53030
β-ACTIN	Mouse	1:10000	Sigma, A1978
ACADL	Rabbit	1:500	Abcam, ab74109
ACADM	Rabbit	1:5000	Abcam, ab108192
ACC1	Rabbit	1:1000	Cell Signaling, 3676
ACC2	Rabbit	1:1000	Cell Signaling, 8578
CD36	Rabbit	1:500	Abcam, ab133625
CPT1A	Rabbit	1:2000	Proteintech,15184-1-ap
G6PD	Rabbit	1:1000	Abcam, ab210702
GAPDH	Mouse	1:5000	Merck, MAB374
GFAT1	Rabbit	1:1000	Proteintech, 14132-1-AP
GFAT2	Rabbit	1:500	Proteintech, 15189-1-AP
GLUT1	Mouse	1:1000	Abcam, ab40084
GLUT4	Mouse	1:500	Abcam, ab35826
HDAH	Rabbit	1:2000	Abcam, ab107260
HK I	Mouse	1:500	Thermo Fisher, MA5-15680
HK II	Rabbit	1:1500	Cell signalling, 2867s (C64G5)
LDHA	Rabbit	1:1000	Proteintech, 21799-1-ap
MCT4	Rabbit	1:750	Abcam, ab74109
OGT	Rabbit	1:2000	Cell signalling, 5368s
OXPHOS COCKTAIL	Mouse	1:250	Abcam, ab110413
PC	Rabbit	1:500	Novus, NBP1-49536SS
PDH_E1-A	Rabbit	1:1000	Abcam, ab155096
PDH_E1-A S293P	Rabbit	1:500	Abcam, ab92696
PDK1	Rabbit	1:1000	Abcam, ab90444
PDK4	Rabbit	1:1000	Abcam, ab63157
PFKM	Mouse	1:1500	Merck, MABS151
PGAM1	Rabbit	1:1000	Abcam, ab96622
PGC1A	Goat	1:4000	Abcam, ab106814
PGC1A S571P	Rabbit	1:4000	R&D systems, AF6650
PGD	Rabbit	1:1000	Abcam, ab129199

PKM1	Rabbit	1:1000	Novus, NBP2-14833
PKM2	Rabbit	1:1000	Sigma, 3198
PPARA	Rabbit	1:1500	Abcam, ab24509
TPI	Goat	1:5000	Abcam, ab28760

1149
1150 ACADL: light-chain acyl-CoA dehydrogenase; ACADM: medium-chain acyl-CoA
1151 dehydrogenase; ACC: acetyl-CoA carboxylase; CD: cluster of differentiation; CPT:
1152 carnitine-palmitoyl transferase; G6PD: glucose-6-phosphate dehydrogenase;
1153 GAPDH: glyceraldehyde-3-phosphate dehydrogenase; GFAT: fructose-6-phosphate
1154 amidotransferase; GLUT: glucose transporter; HDAH: hydroxyacyl-CoA
1155 dehydrogenase; HK: hexokinase; LDH: lactate dehydrogenase; MCT:
1156 monocarboxylate transporter; OGT: O-Linked N-acetylglucosamine transferase;
1157 OXPHOS: oxidative phosphorylation; PC: pyruvate carboxylase; PDH: pyruvate
1158 dehydrogenase; PDK; pyruvate dehydrogenase kinase; PFKM: muscle
1159 phosphofructokinase; PGAM: phosphoglycerate mutase; PGC: peroxisome
1160 proliferator-activated receptor gamma coactivator; PGD: hosphogluconate
1161 dehydrogenase; PKM: pyruvate kinase; PPARA: peroxisome proliferator-activated
1162 receptor alpha; triosephosphate isomerase.